Supplementary Information
Discovery of a hidden transient state in all bromodomain families

Lluís Raich,[a] Katharina Meier,[b] Judith Günther,[c] Clara D. Christ,[c] Frank Noé[a,d,*] and Simon Olsson[a,e*]

[a]*Department of Mathematics and Computer Science, Freie Universität Berlin, 14195 Berlin, Germany.* [b]*Computational Molecular Design, Pharmaceuticals, R&D, 42096 Wuppertal,* Germany. [c]*Computational Molecular Design, Pharmaceuticals, R&D, Bayer AG, 13342 Berlin, Germany*. [d]*Department of Chemistry, Rice University, Houston, TX 77005.* [e]*Current affiliation: Chalmers University of Technology, Department of Computer Science and Engineering, 41258 Gothenburg, Sweden.*

Correspondence: Simon Olsson (simonols@chalmers.se) or Frank Noé (frank.noe@fu-berlin.de)

Table of contents

1. Computational details and methodology

Set up of the systems: bromodomain (BD) structures were obtained from the protein data bank (PDB), using the identifiers and amino acid sequences that are given in Supplementary Table 1. The structures of PHIP(2), BRD1, BAZ2B, TRIM28 and ZMYND11 were shortened in their N- or C-termini to reduce system size. The structure of ZMYND11, from mice and with part of the ZA-loop unresolved, was completed using the Swiss-Model server for homology modeling,[1] modifying the only residue that differs between humans and mice (Ser183Asn). All structures were cleaned of cosolvent molecules and drugs while retaining crystallographic waters. Hydrogen atoms and additional solvent molecules were added using the tleap module of Ambertools[2] (v 19.0), with a distance of 1 nm from any atom of the protein and the simulation box. Counterions were added to neutralize the total charge of the systems and set a 0.15 M NaCl salt concentration. We used the ff14SB[3] force field together with the TIP3P[4] water model to describe the solute and the solvent, respectively. This force field has been previously used to successfully compute protein-ligand affinities in BRD4(1), with errors below 3 kcal/mol.[5]

Simulation details: molecular dynamics simulations were carried out with the OpenMM[6] software (v 7.4.0). A Langevin integrator with a 1 ps friction coefficient and a Monte Carlo barostat were used to maintain the temperature and pressure of the systems at 300 K and 1 bar. Long-range electrostatics were computed using the Particle-Mesh Ewald scheme, and van der Waals interactions were truncated with a 1 nm cutoff. A hydrogen mass repartition with a factor of 2 –including both solute and solvent atoms– was used to increase the integration time step up to 4 fs, constraining the lengths of all bonds. Multiple 1 µs trajectories were ran for each BD, with an initial minimization and 5 additional nanoseconds of equilibration for each trajectory. Frames were saved every 100 ps, including all atoms of the system. As an initial sampling strategy, for each BD we ran 4 trajectories of 250 ns at a higher temperature, two at 350 K and two at 375 K, aiming to overcome high energy barriers and identify states that could be potentially relevant. From these simulations we selected snapshots based on C_α RMSD (root-mean-square deviation; with the crystallographic structure as reference) to run the production simulations at 300 K, with an upper bound of 0.28 nm to avoid selecting states that are too different from the native. The structures were taken in equally-sized steps along the RMSD range. It is worth noting that our findings are not directly depending on this particular protocol, and alternative sampling strategies such as replica exchange or accelerated molecular dynamics can also be employed to generate the initial "seed" structures for the unbiased simulations. The structure of ZMYND11 was not forced with the temperature jump since it was already in the open state and part of the ZA-loop was modeled. An adaptive sampling strategy was adopted afterwards, estimating preliminary Markov state models and selecting snapshots focused on the region of interest. Trajectories were superimposed onto the crystallographic structure based on C_α RMSD using the tleap module, and all solvent atoms and ions were stripped for the subsequent analyses.

Family	I	II	III	IV
BD name	CECR2	BRD4(1)	PHIP(2)	BRD1
PDB id	3NXB	5ULA	3MB3	3RCW
N-terminus	Asp438	Asn44	Ala1320	Thr565
C-terminus	Lys537	Asn162	Leu1422	Val670
Trajectories (µs)	40	64	60	40

Family	V	VI	VII	VIII
BD name	BAZ2B	TRIM28	ZMYND11	SMARCA2
PDB id	3G0L	2RO1	4N4G	5DKC
N-terminus	Leu1870	Ser697	Gln156	Pro1381
C-terminus	Lys1970	Phe800	Gln256	Lys1490
Trajectories (µs)	40	40	48	60

Supplementary Table 1. Bromodomains, protein data bank identifiers and amino acid sequences used in this work, together with the total number of 1 µs trajectories.

Markov modeling: Markov state models (MSM) were built for each individual BD using the PyEMMA[7] software (v 2.5.7), following well-established workflows and protocols.[8] First, we modeled BRD4(1) taking into account residues Leu67 to Arg113 and using different sets of features, including 41 backbone h-bond distances (between heteroatoms) formed along each trajectory, 1081 C_α pairwise distances, 141 C_α XYZ coordinates and 188 sin/cos backbone torsion angles. Trajectories 17 and 25 were filtered from the total since they are involved in a slow process that is related with the loss of a conserved π-stacking interaction (Tyr97-Tyr139). We used a time-lagged independent component analysis (TICA[9,10]) to reduce the dimensionality of each set of features, using a lag time of 10 ns and taking 6 to 14 components depending on the input features (80 to 95% of cumulative variance). The reduced spaces were clustered using the k-means algorithm with 100 centers, and Bayesian MSMs were built selecting the lag times according to the convergence of the implied timescales (0.1 μs). The models were coarse-grained to two states using Perron cluster cluster analysis (PCCA++) and validated with a Chapman-Kolmogorov (CK) test. Errors in populations, mean first passage times (MFPT) and CK tests were computed using a bootstrapping strategy without replacement (100 rounds for populations and MFPTs; 10 for CK tests), taking 80% of the initial trajectories and fitting a new MSM using the same feature map, clustering and metastable discretization than the MSM with the total set of trajectories. All these models showed a perfect agreement for the prediction of thermodynamic and kinetic properties within statistical uncertainties (Supplementary Figure 1), highlighting the robustness of the results independently of the input features, the number of time-lagged independent components (TICs), clustering and coarse-grain discretization. We also reduced the model of backbone h-bonds from 41 input distances to the two most relevant for describing the first TIC (Phe83-Met107 and Gln84-Gly108 backbone h-bonds), finding that this simplified model captures all the kinetic information of the system along the process. Therefore, we decided to use this intuitive featurization to describe the kinetics of all BDs, aiming to facilitate the interpretation of the models and their mutual comparison.

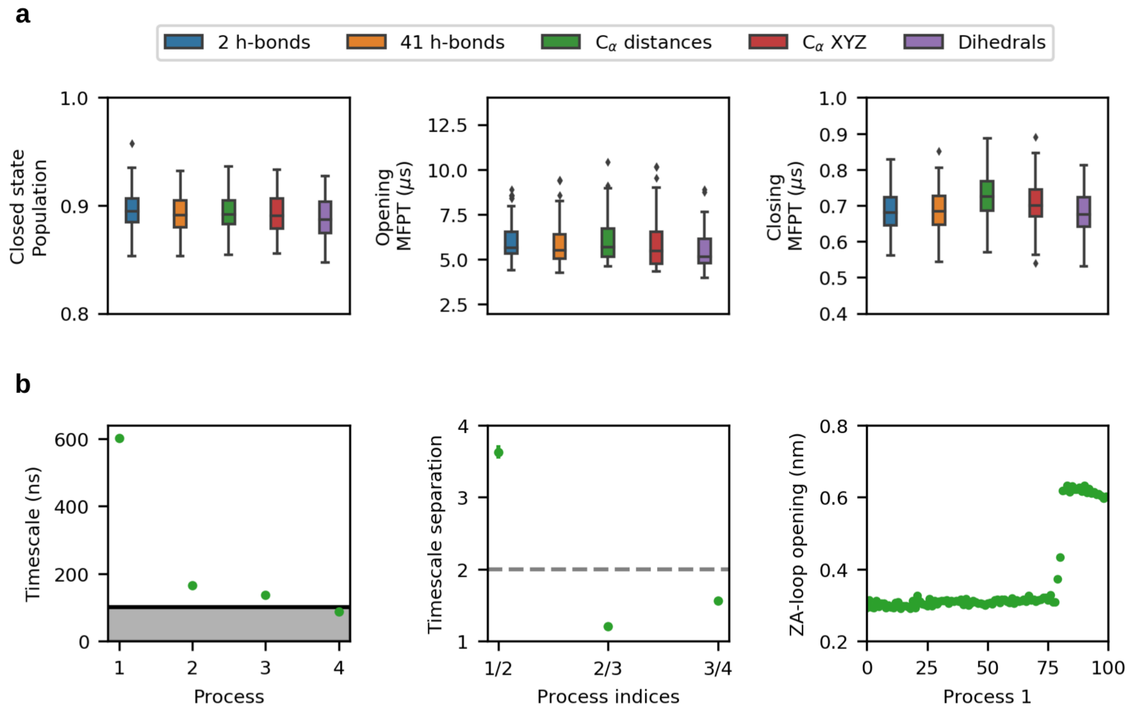

Supplementary Figure 1. Consistency of thermodynamic and kinetic predictions for BRD4(1) with different features. (**a**) Boxplots of a bootstrapped distribution of the closed state population and opening/closing mean first passage time (MFPT) for the two key backbone h-bonds (2 TICs), 41 backbone h-bonds (6 TICs), 1081 C_α distances (13 TICs), 141 C_α XYZ coordinates (14 TICs) and 188 sin/cos backbone dihedral pairs (10 TICs). (**b**) Timescales, spectral gap and ZA-loop opening coordinate along the first process for the system modeled with 1081 C_α distances (13 TICs).

We obtained a general map of TICs using the two key backbone h-bonds and all the trajectories of each BD, defining a lag time of 10 ns and taking both dimensions. The first component represents the breaking of the two h-bonds and is described by the linear combination 2.16·(h-bond 1)+0.20·(h-bond 2), while the second represents the formation of h-bond 1 together with the breaking of h-bond 2 and is described by the linear combination -5.09·(h-bond 1)+5.69·(h-bond 2). This general TIC space was used to build MSMs for each BD. To minimize projection errors in this low-dimensional space, we filtered trajectories that were not reversibly connected in a higher dimensional space made by C_α pairwise distances for each BD, as well as trajectories involved in other slow processes that can not be properly resolved in the reduced space. A pair of metastable states are reversible connected if empirical transitions in both directions have been observed at least once. In total, trajectories 11, 13 and 20 were filtered for CECR2; 17 and 25 for BRD4(1); 1, 14-18, 20, 35, 44, 47, 49, 52, 53 and 57 for PHIP(2); 7, 8, 12, 26, 31, 32, 34, 35 and 39 for BRD1; 9-11, 28, 30-40 for BAZ2B; 37 for TRIM28; 28, 30, 31, 33, 39 and 47 for ZMYND11 and 32, 46, 47, 49, 52 and 53 for SMARCA2. These trajectories involve a diverse set of slow conformational changes, such as the loss of a conserved π-stacking interaction (*e.g.* Tyr471-Tyr513 in CECR2), the perturbation of a conserved hydrophobic residue that is next to the conserved aspartate (*e.g.* Met479 in CECR2), or transitions between different open state conformations of the ZA-loop for BDs that display a high disorder in this region (*e.g.* PHIP(2), BRD1 and BAZ2B). The filtered trajectories were mapped onto the general TIC space and MSMs were built following the same protocols given above for BRD4(1), including an additional convergence test plotting state populations with respect to the lag time. Structural details, kinetic parameters and convergence tests for each of the models are given in Supplementary Figures 2-9. Populations and MFPTs of the bootstrapping distributions are given in Supplementary Tables 2 and 3. Representative structures were selected by taking the most populated cluster of each metastable state, drawing 1000 random snapshots assigned to it. The conformational complexity of TRIM28 prevented us from building a reliable MSM with the acquired simulation data, and thus we only provide evidence of metastability for the open state.

Analysis of crystal structures: bromodomain structures of the Pfam[11] database (PF00439) were downloaded from the PDB and superimposed with Theseus[12] (v 3.3.0), using Muscle (v 3.8.1) for the alignment of sequences. This superimposition and alignment was used to identify the key residues of each BD that are involved in the two backbone h-bonds, and we subsequently computed their distances using MDtraj. Due to ambiguity in the sequence alignment, we manually inspected the structures of all outliers (half of the standard deviation above the median), and in the case of a misassignment we recalculated h-bond distances updating the key residues. In ZMYND11 the identification of such residues is not clear given that in the experimental structures the ZA-loop is either completely unresolved (*e.g.* PDB 4N4I) or partially resolved and in a very open state (PDB 4N4G). The only requirement for the h-bond 1 acceptor residue is that it has to be non-polar and preferably hydrophobic, since it should be bound in the hydrophobic core of the protein when closed. For this reason, we selected Gly180 to act as acceptor for h-bond 1, as it is the only neutral residue in the central part of the ZA-loop that is resolved (PDB 4N4G). Supplementary Figure 18 shows the projection of all structures onto the raw free energy landscape of each BD along the two key h-bonds. Supplementary Figure 19 shows four experimental structures of BDs lacking the conserved aspartate, with different amino acids (Ala, Ser, Trp and Thr) at the critical position. A table with all PDB identifiers, residues and distances is provided as online material.

Additional details: the visual inspection of structures and the production of figures were done with VMD[13] (v 1.9.3). MDtraj[14] (v 1.9.3) was used for computing structural parameters, including h-bond analyses and solvent accessible surface areas (SASA). Plumed[15] (v 2.5.3) was used for the prediction of chemical shifts within the CAMSHIFT[16] model. NGLview[17] (v 2.7.1) was used to visualize structures during preliminary analyses. All plots were done with Matplotlib (v 3.1.1) and the seaborn library (v 0.9.0) was used for the distributions –with a Gaussian kernel density estimation– and boxplots.

MDpocket[18] (v 3.0) was used to detect small molecule binding sites and to calculate pocket volumes (Supplementary Figure 15). Acetyl-lysine pockets were manually selected from each closed state using frequency maps at isovalues of 0.5, corresponding to at least 50% of pocket opening in all frames. For PHIP(2) the acetyl-lysine pocket was selected at isovalues of 0.25 given its low opening frequency, discarding parts that extend towards the connection between the ZA-loop and the α_A helix. For ZMYND11 we selected the principal cryptic pocket of the open state since the closed state is never fully formed and thus the acetyl-lysine pocket is not defined (see Supplementary Figure 15b). The shrinking of pockets was estimated computing their volumes with the structures of both closed and open states, discarding null volumes that result as a consequence of pocket parameters (minimum of 35 alpha spheres and 3 Å radius). Note that the evaluation of acetyl-lysine pocket volumes with the structures of the open state gives an estimate of their occlusion as a consequence of the conformational change.

Druggability scores were computed with Fpocket[19] (v 3.0), which generates several pockets for each structure. We filtered the pockets of interest based on the contacts of their alpha spheres with specific residues, with a distance cutoff of 0.35 nm. Specifically, for the acetyl-lysine pocket in the closed state we used residues Phe459 *and* Cys510 (residues of CECR2 in 3NXB, analogous residues in the other BDs), and for the cryptic pockets in the open state we used residues Asp480 *or* Ile481, allowing to filter pockets located beneath the ZA-loop. For ZMYND11 we used residues Val198 *and* Leu223 for both states since they are essentially open. We note that several cryptic pockets communicate with the (partially occluded) acetyl-lysine pocket in the open state, connected by narrow channels, thereby mixing scores of pockets that are essentially different. We also find cases in which the opposite happens, it is, pockets that should be considered as a unique entity (*e.g.* the acetyl-lysine pocket) are split into subpockets, leaving small cavities with low scores that shift the distributions.

The sequence alignment in Figure 1b was done using the STAMP[20] algorithm implemented in VMD, which takes advantage of structural information. First, we aligned the ZA-loop segments of all minimized structures, resulting an alignment with several gaps given the unusual conformations of TRIM28 and ZMYND11. In a second step, we refined the sequence of ZMYND11 manually, filling the gaps of the backbone h-bond acceptors with the nearest residues in the alignment (Gly180 and Lys181). Finally, we realigned the entire sequence of TRIM28 using ClustalX[21] (v 2.1) and removed gaps in the entire alignment that lead to single amino acids disconnected.

2. Markov state models of each bromodomain family

In this section we provide a summary of the Markov state models of each BD family (Supplementary figures 2 to 9). All figures are organized identically with 5 different subsections, apart from TRIM28 and ZMYND11. The first subsection (a) shows the general BD fold and a close view of the key region for the two metastable states, closed and open, colored in cyan and yellow respectively. The second and the third (b and c) show structural parameters, free energy profiles and mean-first passage times that characterize the conformational change. The fourth (d) shows a superposition of the predicted closed states and their pocket frequency maps with experimental structures of BDs complexed with drugs. Finally, the fifth subsection (e) shows convergence tests for the MSMs, including the Chapman-Kolmogorov test and time convergence of populations and timescales. TRIM28 and ZMYND11 lack convergence tests given that we do not use their MSMs to report populations nor timescales. Furthermore, TRIM28 lacks the section of pocket frequency maps as it does not display noticeable pockets in the region of interest. Instead of this, we provide the evolution of three selected trajectories that show clear metastability in the open state.

We note that for CECR2, BRD4(1) and SMARCA2 systems we generally see a clear two-state behavior, with very stable structures and few alternative states, resulting in well converged models. On the other hand, PHIP(2), BRD1 and BAZ2B systems have more complex conformational landscapes, and thus the two-state approximation and the simplified featurization may affect the robustness of the reported rates and state populations. This can be observed in the Chapman-Kolmogorov tests of these systems (Supplementary Figures 4-6 panel e), which show large confidence intervals and a moderate agreement between the predicted and estimated decay of probability densities. Nevertheless, all models clearly resolve the metastability of the closed and open states of the ZA-loop, confirming its kinetic relevance.

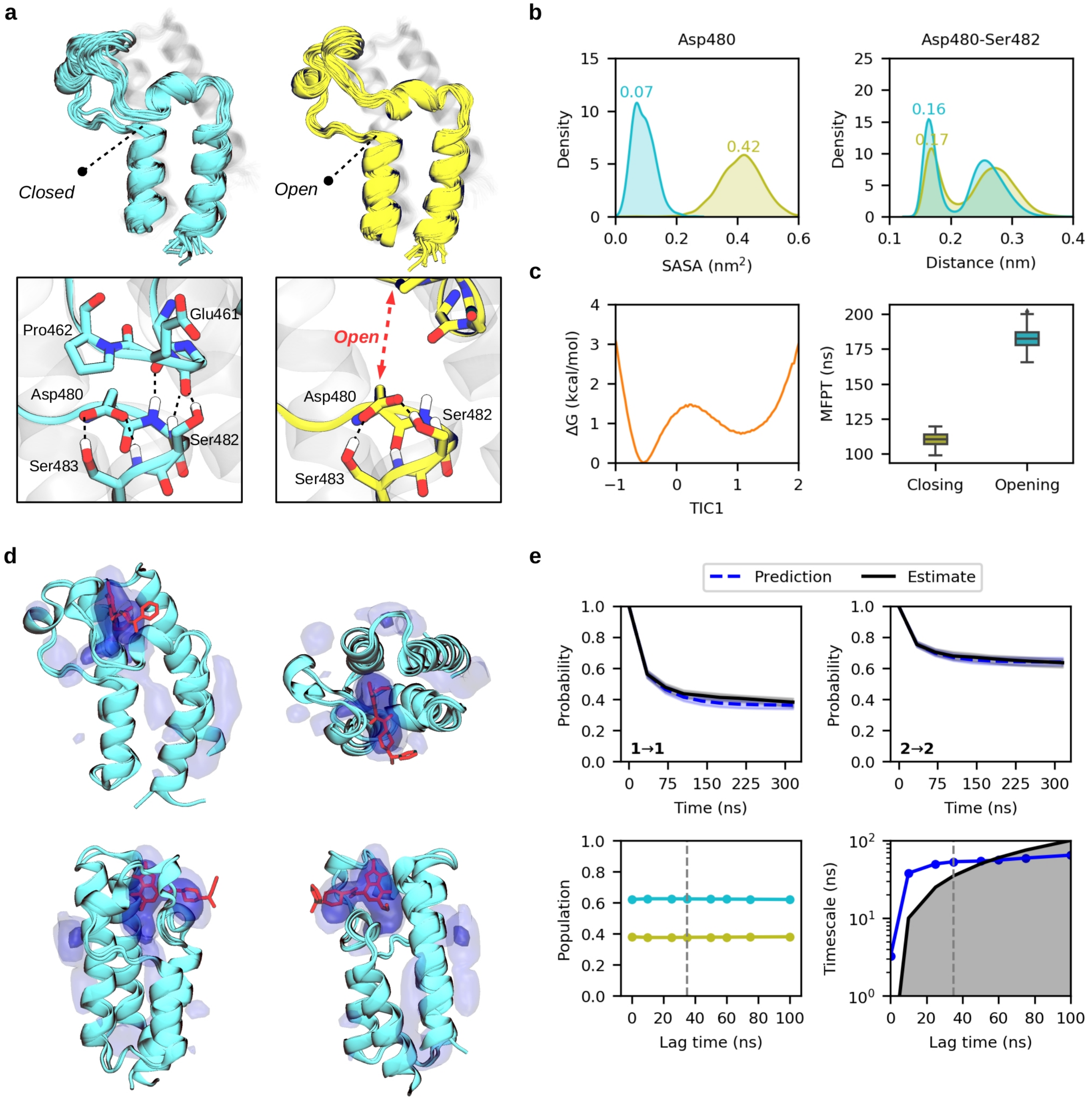

Supplementary Figure 2. The hidden conformational state in CECR2 of family I. (**a**) Ensemble of structures of the “closed” crystal-like state (cyan) and the “open” state (yellow). A close view of the opening region is represented below, highlighting Asp480. (**b**) Distribution of the Asp480 solvent accessible surface area (SASA) and closest distance between Asp480-Ser482 side chains for the two metastable states. (**c**) Reweighted free energy profile along the second component (TIC1) and boxplot with the opening and closing mean first passage times. (**d**) Pocket frequency maps of the closed state superposed with an X-ray structure (PDB 5V84) in complex with a drug molecule shown in red. Isosurfaces are given at 0.25 (light) and 0.50 (intense) values. (**e**) Chapman-Kolmogorov test for the two states (1 open, 2 closed), and convergence of populations and timescales with respect to the lag time. Vertical dashed lines indicate the lag time used to build the MSM (35 ns).

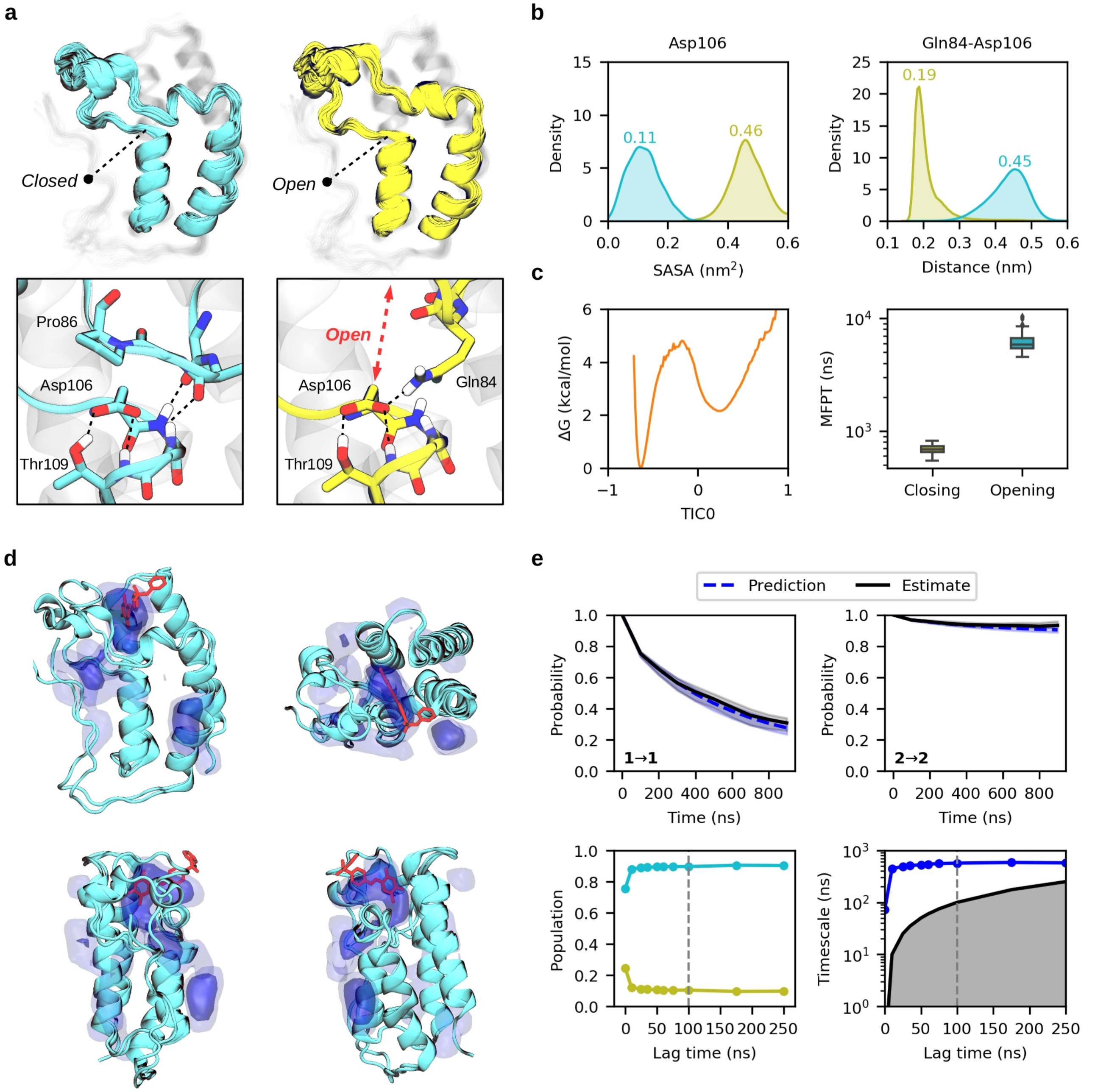

Supplementary Figure 3. The hidden conformational state in BRD4(1) of family II. (**a**) Ensemble of structures of the "closed" crystal-like state (cyan) and the "open" state (yellow). A close view of the opening region is represented below, highlighting Asp106. (**b**) Distribution of the Asp106 solvent accessible surface area (SASA) and closest distance between Gln86-Asp106 side chains for the two metastable states. (**c**) Reweighted free energy profile along the first component (TIC0) and boxplot with the opening and closing mean first passage times. (**d**) Pocket frequency maps of the closed state superposed with an X-ray structure (PDB 4NUD) in complex with a drug molecule shown in red. Isosurfaces are given at 0.25 (light) and 0.50 (intense) values. (**e**) Chapman-Kolmogorov test for the two states (1 open, 2 closed), and convergence of populations and timescales with respect to the lag time. Vertical dashed lines indicate the lag time used to build the MSM (100 ns).

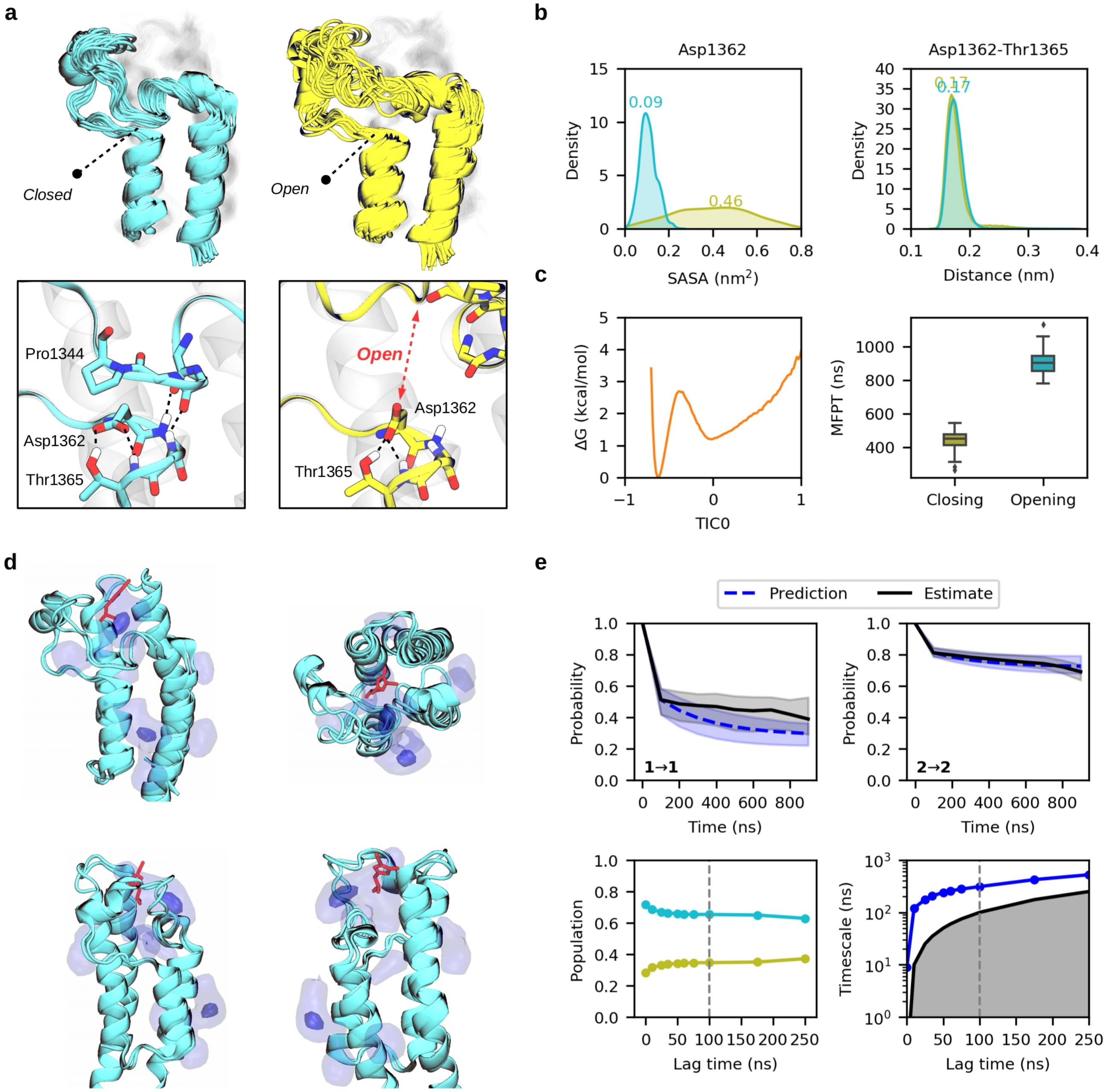

Supplementary Figure 4. The hidden conformational state in PHIP(2) of family III. (**a**) Ensemble of structures of the “closed” crystal-like state (cyan) and the “open” state (yellow). A close view of the opening region is represented below, highlighting Asp1362. (**b**) Distribution of the Asp1362 solvent accessible surface area (SASA) and closest distance between Asp1362-Thr1365 side chains for the two metastable states. (**c**) Reweighted free energy profile along the first component (TIC0) and boxplot with the opening and closing mean first passage times. (**d**) Pocket frequency maps of the closed state superposed with an X-ray structure (PDB 5ENF) in complex with a molecular fragment shown in red. Isosurfaces are given at 0.25 (light) and 0.50 (intense) values. (**e**) Chapman-Kolmogorov test for the two states (1 open, 2 closed), and convergence of populations and timescales with respect to the lag time. Vertical dashed lines indicate the lag time used to build the MSM (100 ns).

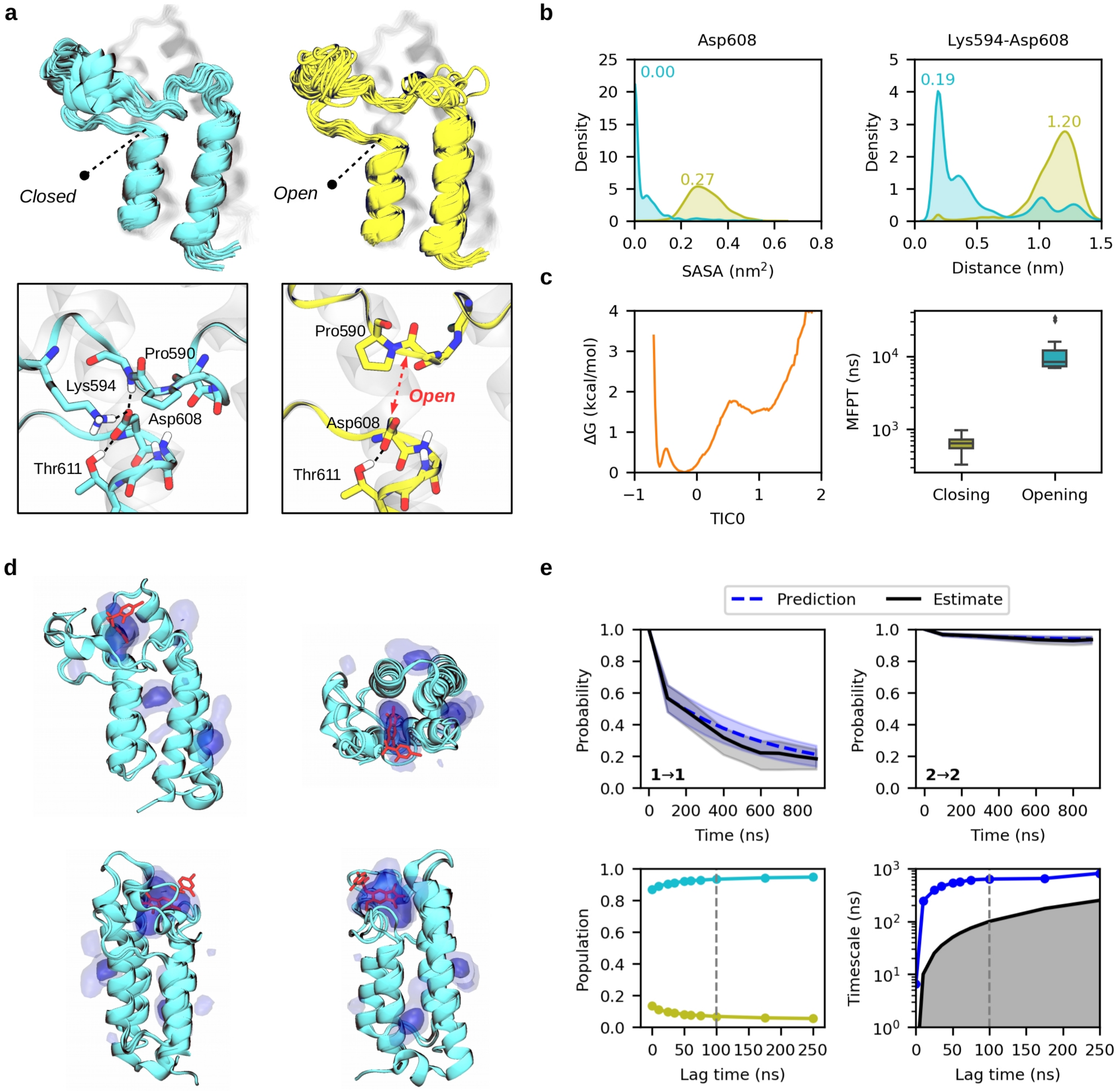

Supplementary Figure 5. The hidden conformational state in BRD1 of family IV. (**a**) Ensemble of structures of the “closed” crystal-like state (cyan) and the “open” state (yellow). A close view of the opening region is represented below, highlighting Asp608. (**b**) Distribution of the Asp608 solvent accessible surface area (SASA) and closest distance between Lys594-Asp608 side chains for the two metastable states. (**c**) Reweighted free energy profile along the first component (TIC0) and boxplot with the opening and closing mean first passage times. (**d**) Pocket frequency maps of the closed state superposed with an X-ray structure (PDB 5FG6) in complex with a drug molecule shown in red. Isosurfaces are given at 0.25 (light) and 0.50 (intense) values. (**e**) Chapman-Kolmogorov test for the two states (1 open, 2 closed), and convergence of populations and timescales with respect to the lag time. Vertical dashed lines indicate the lag time used to build the MSM (100 ns).

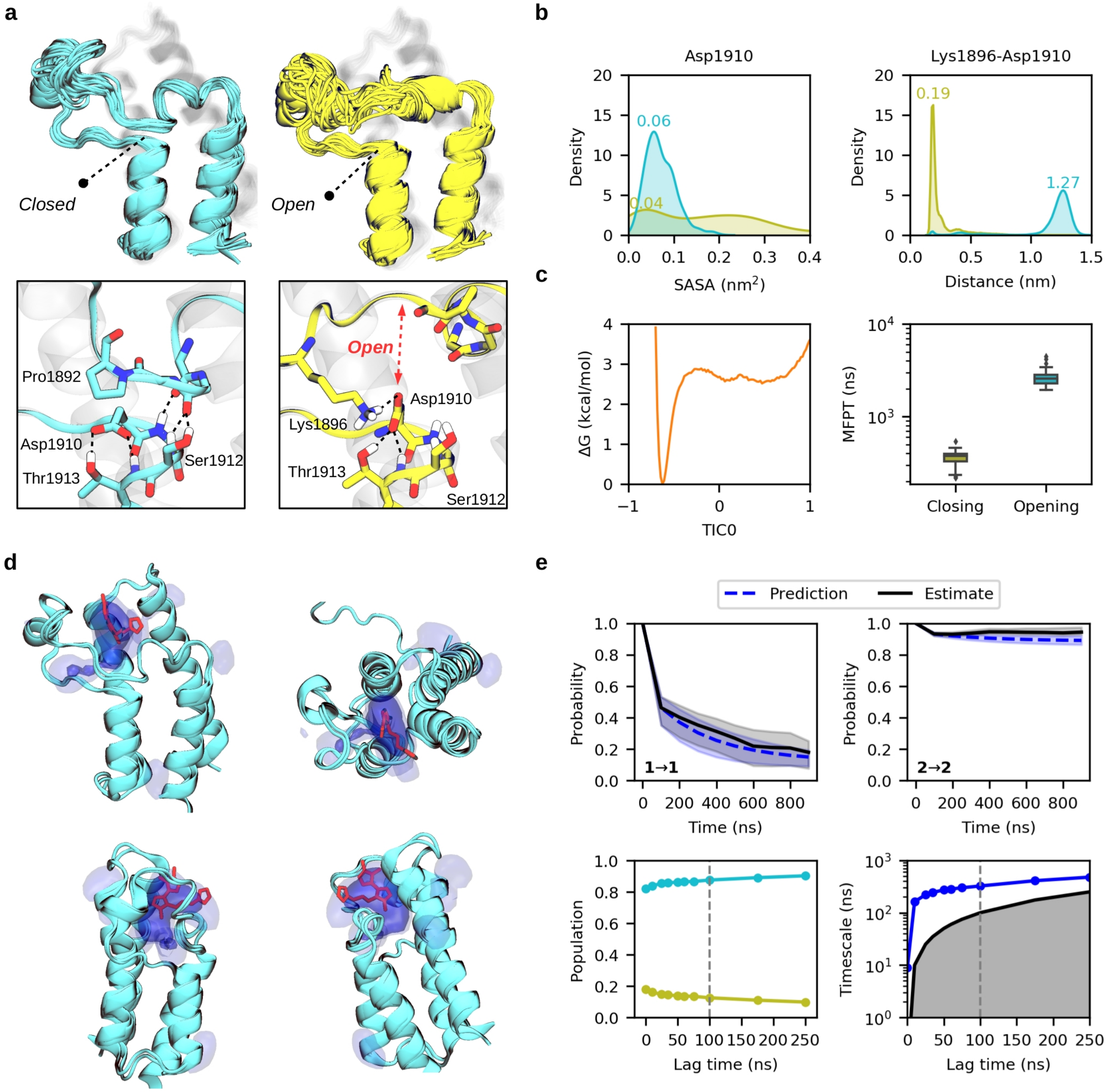

Supplementary Figure 6. The hidden conformational state in BAZ2B of family V. (**a**) Ensemble of structures of the "closed" crystal-like state (cyan) and the "open" state (yellow). A close view of the opening region is represented below, highlighting Asp1910. (**b**) Distribution of the Asp1910 solvent accessible surface area (SASA) and closest distance between Lys1896-Asp1910 side chains for the two metastable states. (**c**) Reweighted free energy profile along the first component (TIC0) and boxplot with the opening and closing mean first passage times. (**d**) Pocket frequency maps of the closed state superposed with an X-ray structure (PDB 3Q2F) in complex with a drug molecule shown in red. Isosurfaces are given at 0.25 (light) and 0.50 (intense) values. (**e**) Chapman-Kolmogorov test for the two states (1 open, 2 closed), and convergence of populations and timescales with respect to the lag time. Vertical dashed lines indicate the lag time used to build the MSM (100 ns).

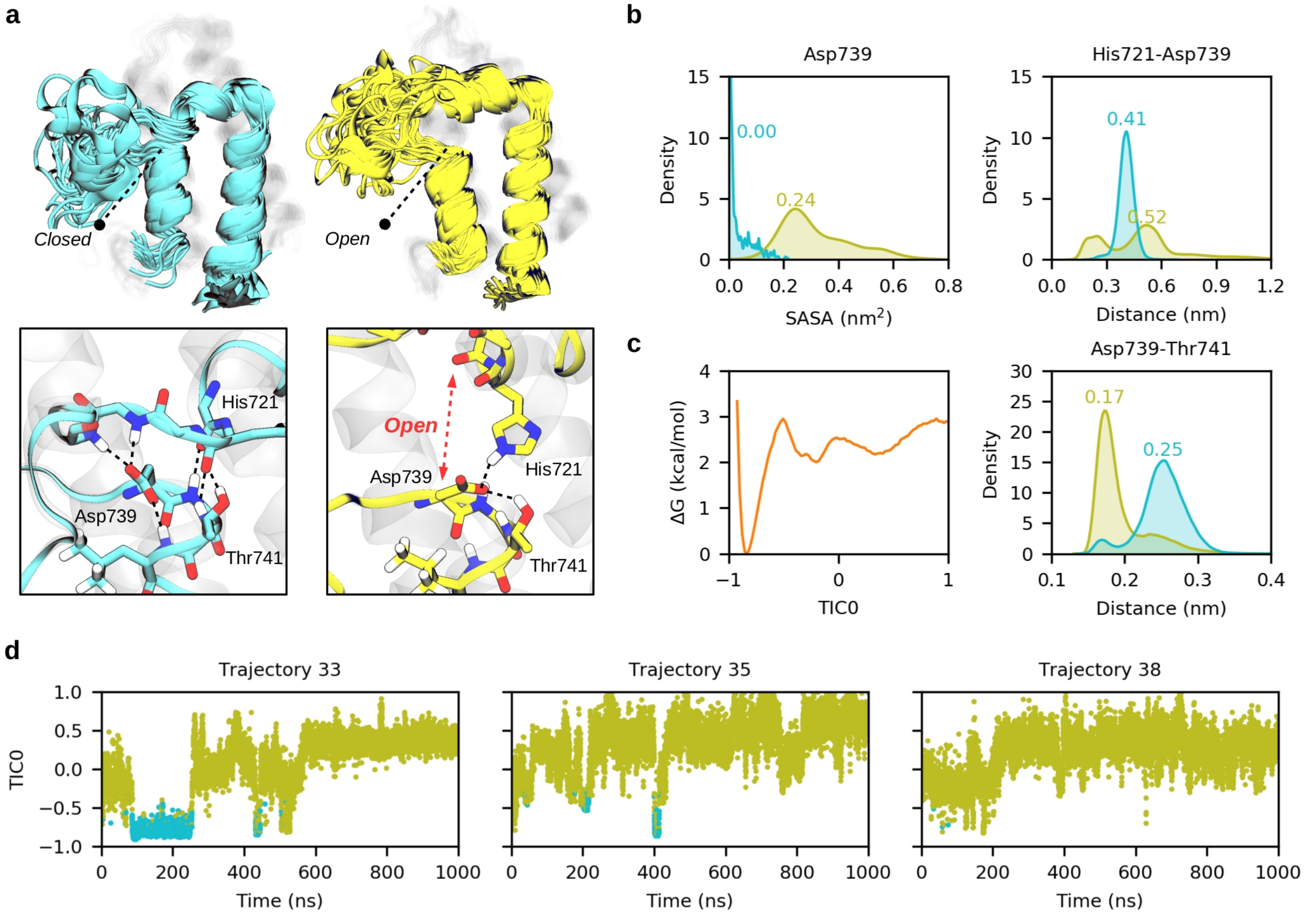

Supplementary Figure 7. The hidden conformational state in TRIM28 of family VI. (**a**) Ensemble of structures of the “closed” crystal-like state (cyan) and the “open” state (yellow). A close view of the opening region is represented below, highlighting Asp739. (**b**) Distribution of the Asp739 solvent accessible surface area (SASA) and closest distance between His721-Asp739 side chains for the two metastable states. (**c**) Raw free energy profile along the first component (TIC0) and distribution of the Asp739-Thr741 closest distance for the two metastable states. (**d**) Evolution of TIC0 along three independent 1 µs trajectories, showing clear metastability between the two states.

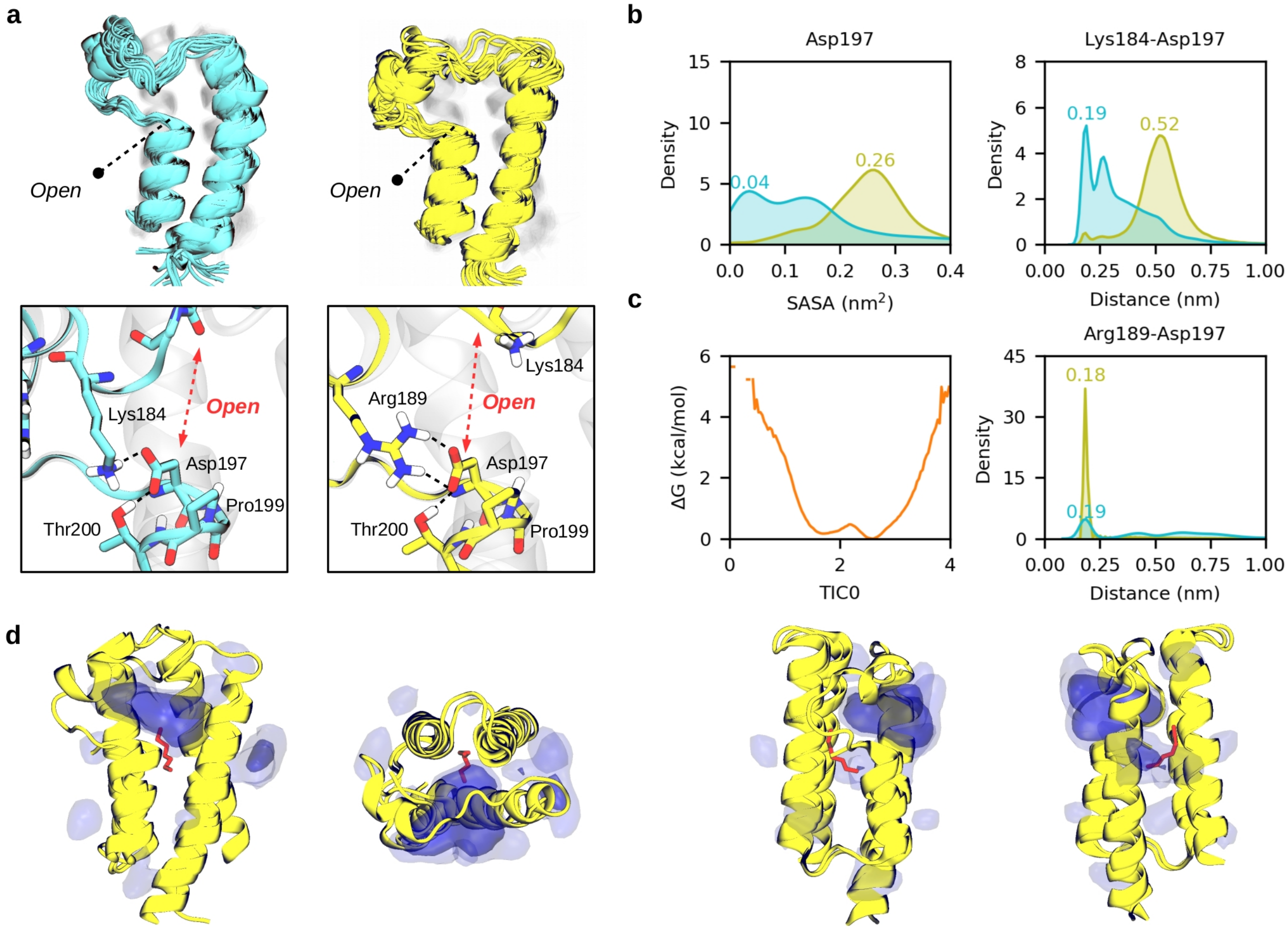

Supplementary Figure 8. The hidden conformational state in ZMYND11 of family VII. (**a**) Ensemble of structures of the “semiclosed” state (cyan) and the “open” crystal-like state (yellow). A close view of the opening region is represented below, highlighting Asp197. (**b**) Distribution of the Asp197 solvent accessible surface area (SASA) and closest distance between Lys184-Asp197 side chains for the two metastable states. (**c**) Raw free energy profile along the first component (TIC0) and distribution of the Arg189-Asp197 closest distance for the two metastable states. (**d**) Pocket frequency maps of the open state superposed with an X-ray structure (PDB 4N4I) in complex with a polyethylene glycol molecule shown in red. Isosurfaces are given at 0.25 (light) and 0.50 (intense) values.

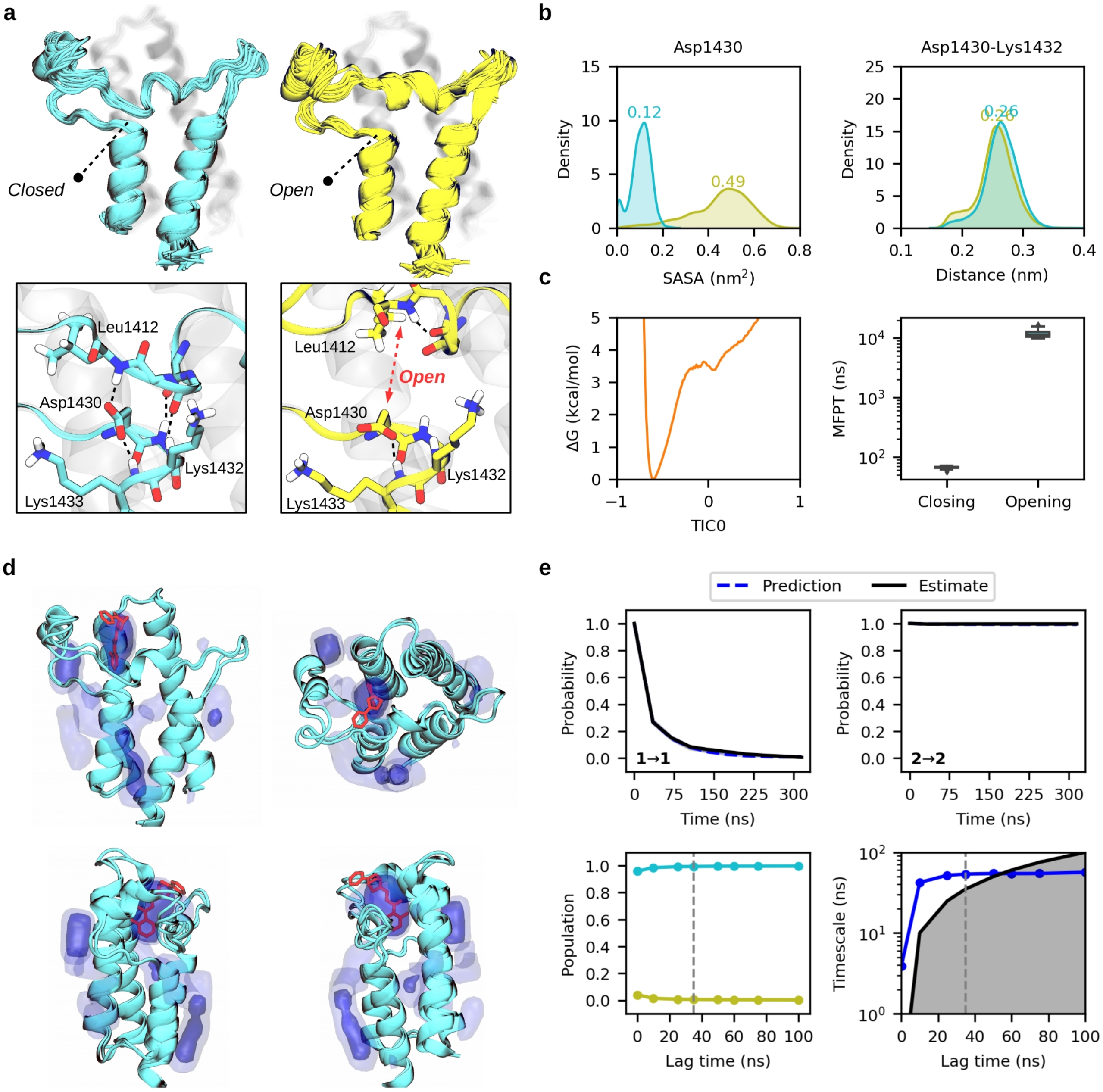

Supplementary Figure 9. The hidden conformational state in SMARCA2 of family VIII. (**a**) Ensemble of structures of the "closed" crystal-like state (cyan) and the "open" state (yellow). A close view of the opening region is represented below, highlighting Asp1430. (**b**) Distribution of the Asp1430 solvent accessible surface area (SASA) and closest distance between Asp1430 -Lys1432 side chains for the two metastable states. (**c**) Reweighted free energy profile along the first component (TIC0) and boxplot with the opening and closing mean first passage times. (**d**) Pocket frequency maps of the closed state superposed with an X-ray structure (PDB 5DKC) in complex with a drug molecule shown in red. Isosurfaces are given at 0.25 (light) and 0.50 (intense) values. (**e**) Chapman-Kolmogorov test for the two states (1 open, 2 closed), and convergence of populations and timescales with respect to the lag time. Vertical dashed lines indicate the lag time used to build the MSM (35 ns).

	CECR2		BRD4(1)		PHIP(2)	
	Open	Closed	Open	Closed	Open	Closed
Samples	100	100	100	100	100	100
Mean	0.38	0.62	0.10	0.90	0.34	0.66
SD	0.01	0.01	0.02	0.02	0.04	0.04
Min	0.34	0.59	0.06	0.85	0.21	0.59
25%	0.37	0.61	0.09	0.88	0.32	0.63
Median	0.38	0.62	0.10	0.90	0.34	0.66
75%	0.39	0.63	0.12	0.91	0.37	0.68
Max	0.41	0.66	0.15	0.94	0.41	0.79

	BRD1		BAZ2B		SMARCA2	
	Open	Closed	Open	Closed	Open	Closed
Samples	100	100	100	100	100	100
Mean	0.07	0.93	0.13	0.87	0.01	0.99
SD	0.02	0.02	0.02	0.02	0.00	0.00
Min	0.01	0.87	0.07	0.84	0.00	0.99
25%	0.05	0.92	0.12	0.86	0.01	0.99
Median	0.07	0.93	0.13	0.87	0.01	0.99
75%	0.08	0.95	0.14	0.88	0.01	0.99
Max	0.13	0.99	0.16	0.93	0.01	1.00

Supplementary Table 2. Bootstrapping distribution of populations for each BD, including the number of samples, mean and standard deviation (SD), minimum and maximum values of the distribution, median and the 25-75th percentiles.

	CECR2		BRD4(1)		PHIP(2)	
	Closing	Opening	Closing	Opening	Closing	Opening
Samples	100	100	100	100	100	100
Mean	110	183	690	6129	441	907
SD	4	7	61	1233	51	70
Min	99	166	545	4564	262	781
25%	107	178	651	5408	410	856
Median	110	182	688	5864	449	903
75%	114	187	732	6667	477	945
Max	120	202	818	10418	544	1131

	BRD1		BAZ2B		SMARCA2	
	Closing	Opening	Closing	Opening	Closing	Opening
Samples	100	100	100	100	100	100
Mean	645	9936	364	2620	67	11784
SD	117	4096	57	455	3	1522
Min	327	6998	218	1930	56	9852
25%	551	7312	329	2284	66	10420
Median	643	8344	377	2585	68	11523
75%	721	12107	395	2809	69	12609
Max	971	33633	537	4487	71	16571

Supplementary Table 3. Bootstrapping distribution of mean-first passage times (ns) for each BD, including the number of samples, mean and standard deviation (SD), minimum and maximum values of the distribution, median and the 25-75th percentiles.

3. Analysis of free energy landscapes

In this section we analyze the empirical free energy landscapes of each key h-bond and a contact distance that qualitatively describes the ZA-loop opening (Supplementary Figures 10 and 11). This contact distance is defined as the minimum distance between a segment of backbone heavy atoms of the ZA-loop and all atoms of the conserved aspartate. The segment extends from the ZA channel to a conserved hydrophobic residue that wraps the ZA-loop with the α_B helix (Glu461-Ile475 in CECR2; analogous residues in the other BDs).

The free energy landscapes of h-bond 1 and the ZA-loop opening (Supplementary Figure 10) display four interesting points to note. First, all maps show basins in the upper right quadrant (breaking of the h-bond and ZA-loop opening) except for CECR2, whose basin is more centered in the upper left quadrant (opening of the ZA-loop without breaking the h-bond). Second, the basins of ZMYND11 are found at values above 1 nm for the h-bond axis, highlighting that it does not form. Third, BRD1 has a low energy region that encompasses an equilibrium between formed and broken h-bond in the closed state. Fourth, most of the BDs substantially explore the upper left quadrant without showing notable minima, indicating opening events that rapidly close.

Regarding the third point, Supplementary Figure 12 shows detailed structures along the low energy region in BRD1, related with a slight displacement of the ZA-loop towards the α_Z helix. This displacement implies the breaking of the key h-bonds, which are compensated by additional h-bonds that backbone amides of the ZA-loop establish with the conserved aspartate. Interestingly, we found similar interactions in CECR2, PHIP(2), and BAZ2B (lower right quadrant in either Supplementary Figures 10 or 11), resembling the type of interactions that are present in the experimental structures of TRIM28 and all Family VIII members.

Regarding the fourth point, Supplementary Figure 13 shows trajectories of each BD were sporadic openings occur, characterized by narrow and dark peaks. These fast openings are common in all BDs and are generally not metastable. BRD1 is an exception, as it displays two open states that are metastable, with clear basins in the free energy landscape (one at 0.5 nm of h-bond 1 and the other at 1.0 nm; see Supplementary Figure 14). The state at 0.5 nm relaxes within a timescale that is faster than the resolution of the MSM, while the state at 1.0 nm is the slow process resolved by the model. The main difference between the two states is the orientation of the ZA-loop, which points outwards for the fast process and inwards for the slow, occluding the acetyl-lysine pocket.

Supplementary Table 4 reflects some of the points highlighted above, showing for CECR2 a substantial percentage of h-bond 1 in the open state, and for BRD1 a low percentage of the two key h-bonds in the closed state.

	CECR2		BRD4(1)		PHIP(2)		BRD1	
	h-bond 1	h-bond 2	h-bond 1	h-bond 2	h-bond 1	h-bond 2	h-bond 1	h-bond 2
Closed	0.98	0.57	0.96	0.11	0.85	0.51	0.18	0.03
Open	0.22	0.00	0.00	0.00	0.00	0.00	0.00	0.00

	BAZ2B		TRIM28		SMARCA2	
	h-bond 1	h-bond 2	h-bond 1	h-bond 2	h-bond 1	h-bond 2
Closed	0.93	0.28	0.94	0.54	0.82	0.59
Open	0.00	0.00	0.06	0.00	0.00	0.00

Supplementary Table 4. Percentage of frames that fulfill the geometrical criterion of a h-bond (distance$_{\mathrm{NH\cdots O}}$ <= 0.25 nm and angle$_{\mathrm{NHO}}$ >= 120º) for the two key h-bonds and the two metastable states of each BD. ZMYND11 is not included in the analysis because a proline (Pro199) is in place of the residue that acts as donor of h-bond 2.

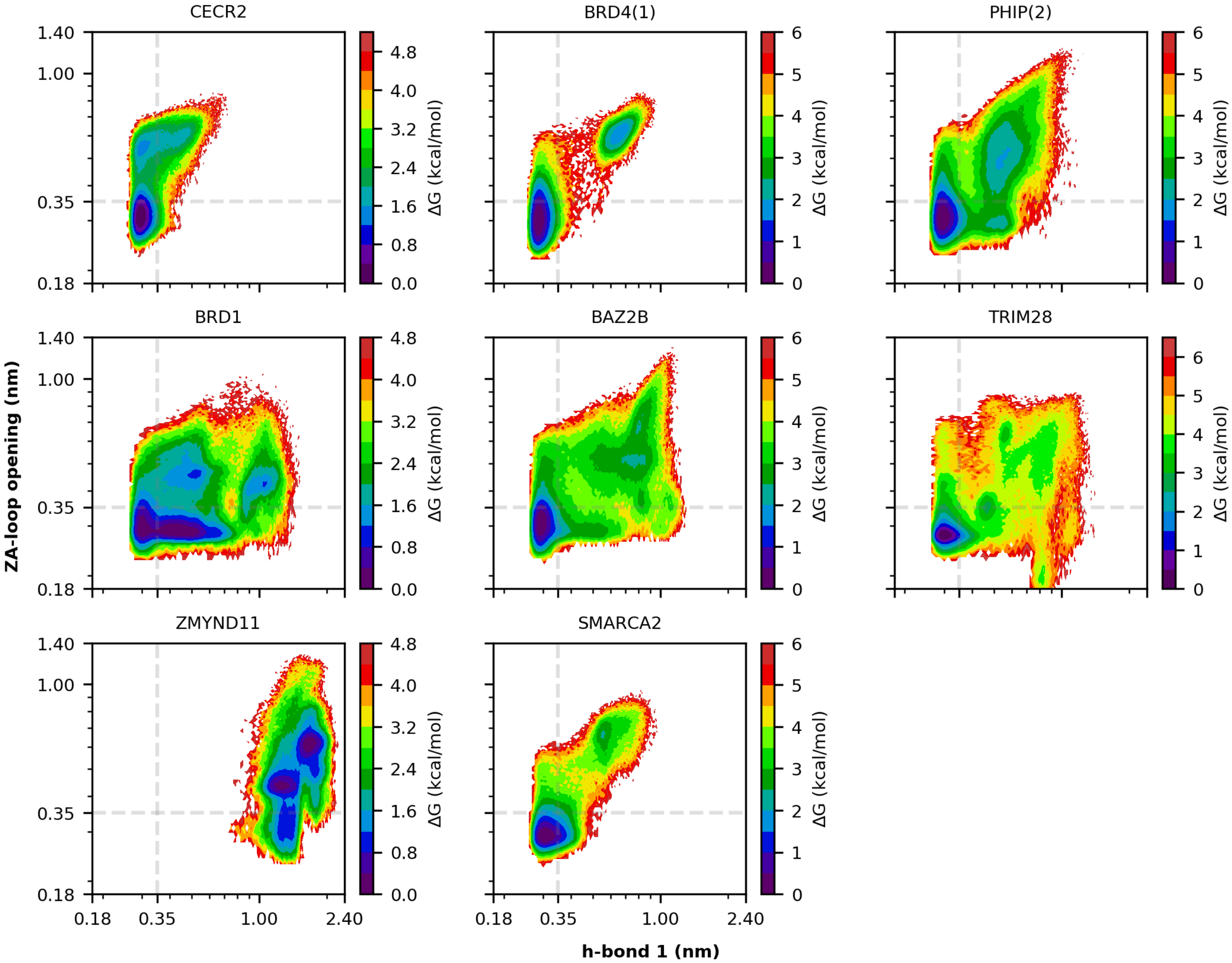

Supplementary Figure 10. Raw free energy landscape of the key h-bond 1 and the ZA-loop opening for each BD. Empirical free energy map computed via projection of all the simulation data onto h-bond 1 and the ZA-loop backbone contacts with the conserved aspartate. Axes are given in a logarithmic scale to facilitate comparison between BDs. Dashed lines indicate a distance of 0.35 nm as an upper bound for h-bond formation, which also represents one of the minimum possible contacts between the ZA-loop and the conserved aspartate.

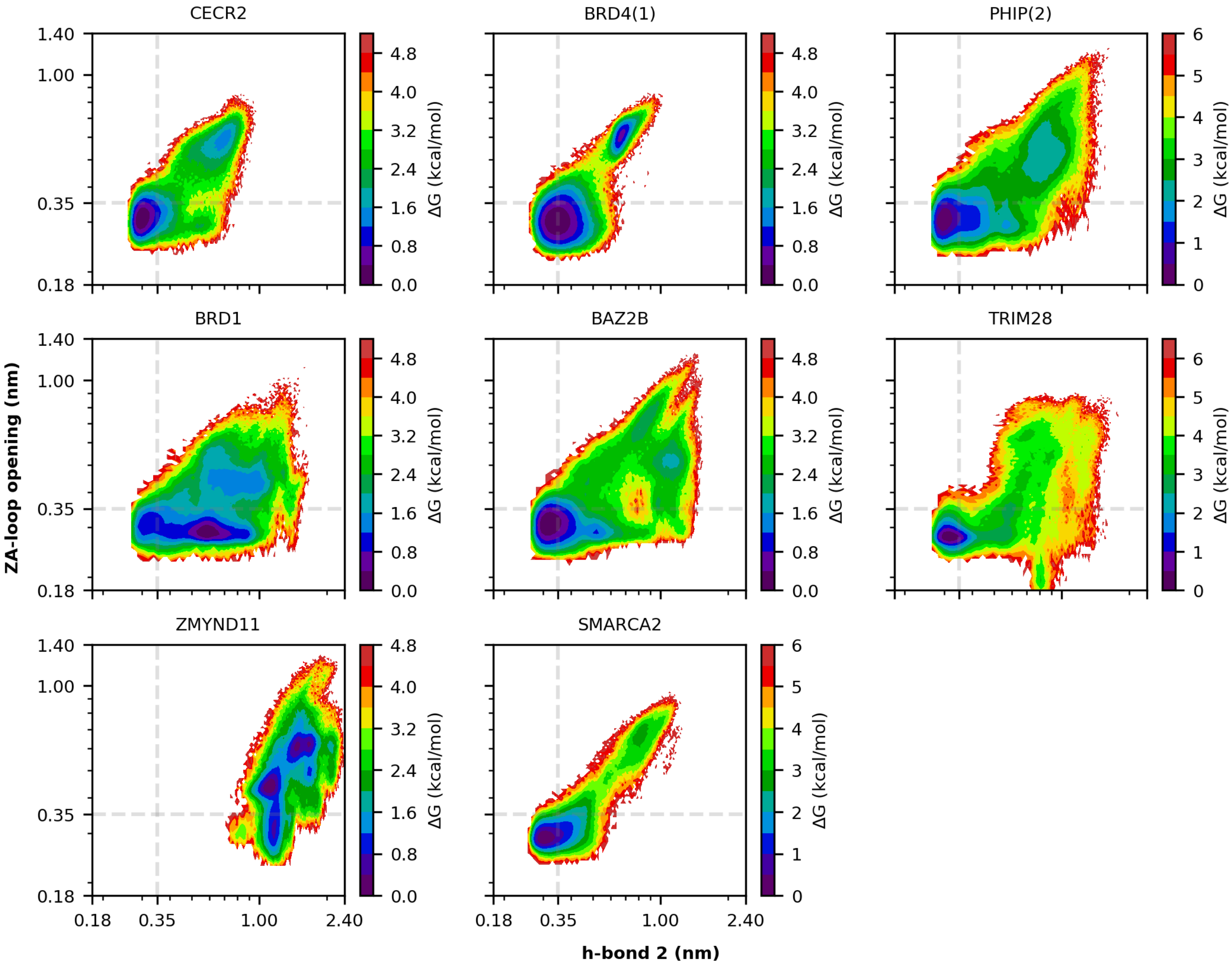

Supplementary Figure 11. Raw free energy landscape of the key h-bond 2 and the ZA-loop opening for each BD. Empirical free energy map computed via projection of all the simulation data onto h-bond 2 and the ZA-loop backbone contacts with the conserved aspartate. Axes are given in a logarithmic scale to facilitate comparison between BDs. Dashed lines indicate a distance of 0.35 nm as an upper bound for h-bond formation, which also represents one of the minimum possible contacts between the ZA-loop and the conserved aspartate.

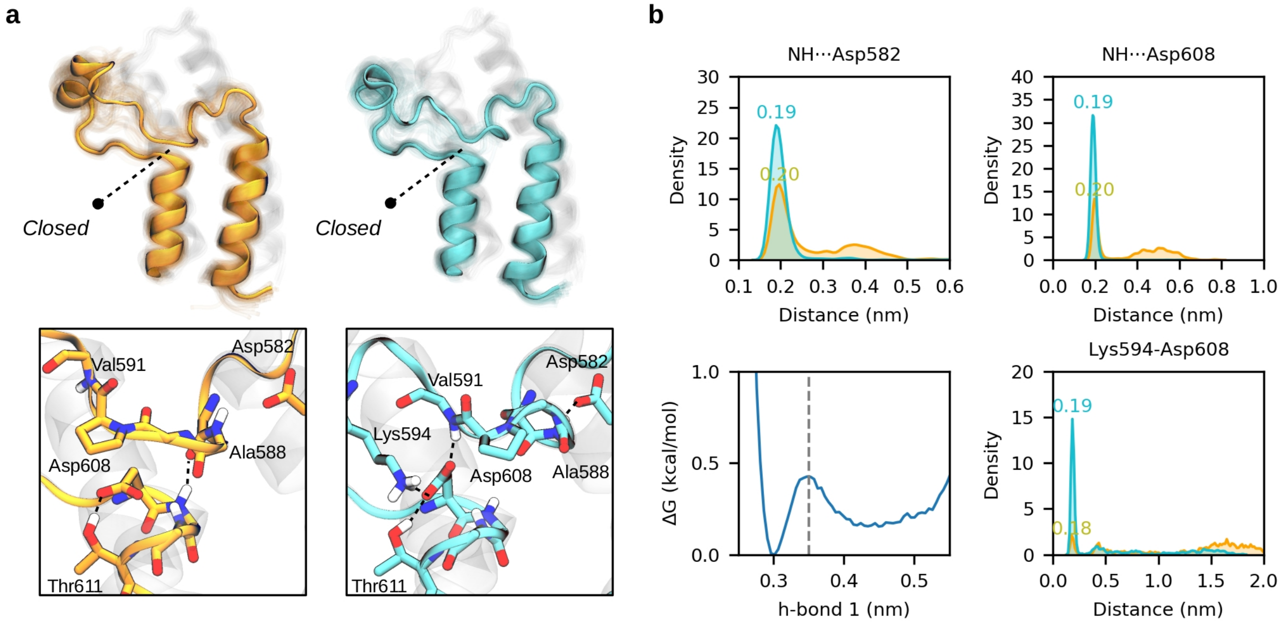

Supplementary Figure 12. Alternative closed state in BRD1 where the ZA-loop slightly displaces towards the α_Z helix. (**a**) Structure of the "closed" crystal-like state (orange) and the alternative closed state in which the ZA-loop is slightly displaced (cyan). A close view of the key region is represented below, highlighting the buried Asp582 and the conserved Asp608, both of which establish h-bonds with different backbone amides of the ZA-loop (mostly the ones of Ala588 and Val591). (**b**) Distribution of the minimum h-bond distance between selected ZA-loop amides and Asp582/Asp608, empirical free energy profile along h-bond 1, and minimum h-bond distance between Lys594 with Asp608 for the two metastable states. Note that the distributions in orange are bimodal and turn nearly unimodal (cyan) due to the conformational change.

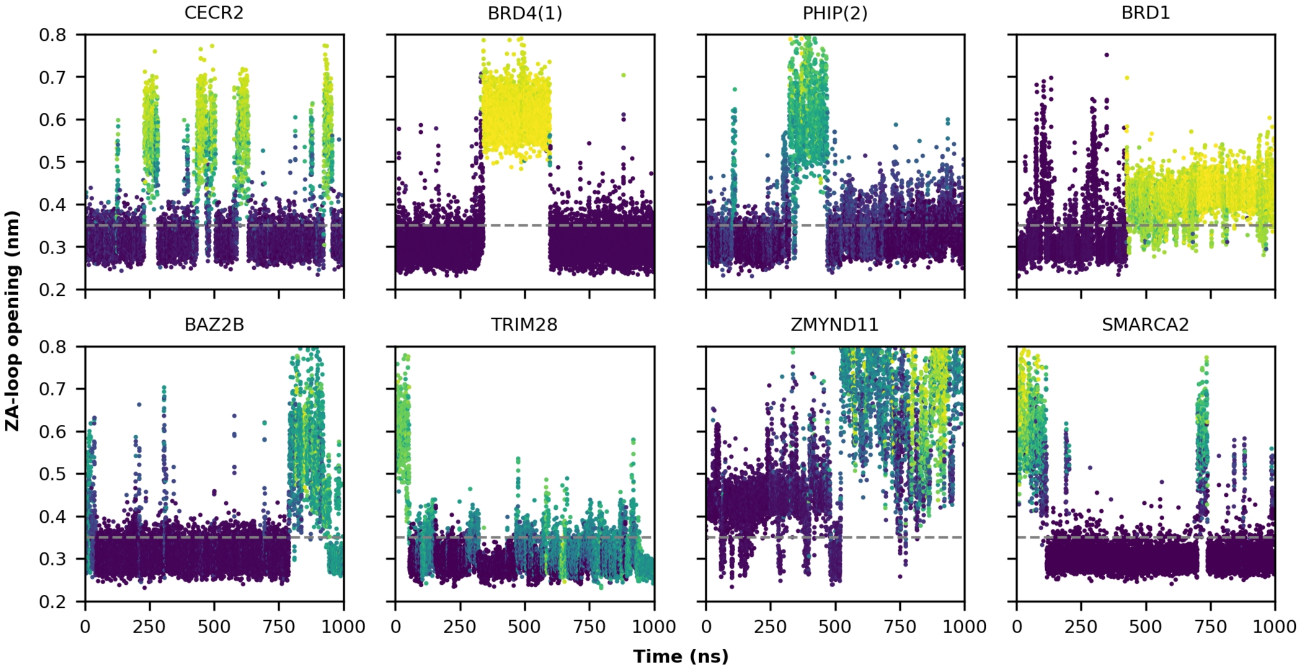

Supplementary Figure 13. Selected trajectories showing sporadic openings of the ZA-loop for each BD. Evolution of the ZA-loop opening contact distance along representative trajectories. Dots are colored according to their membership in the metastable open state characterized by each MSM, with green-yellow regions indicating a high probability and dark regions a low probability. Dashed lines indicate a distance of 0.35 nm as a reference of h-bond contacts. Note the sporadic, narrow and dark peaks that are present in all plots, indicating fast openings that lead to open states that are not metastable. Note as well that in ZMYND11 the closed state show contacts mostly above 0.35 nm, and is therefore only “semiclosed”.

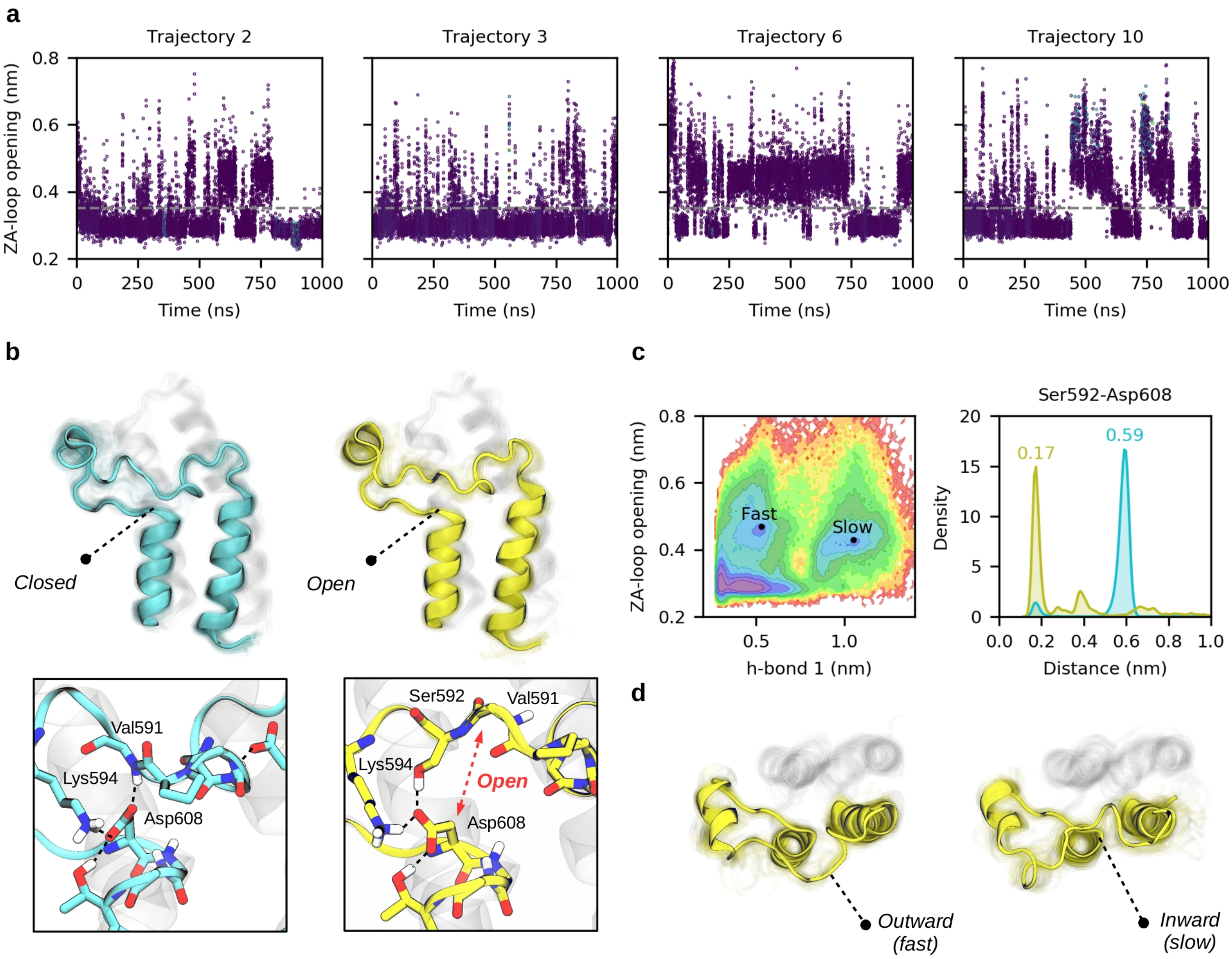

Supplementary Figure 14. Selected trajectories showing sporadic openings of the ZA-loop in BRD1. (**a**) Four different trajectories showing fast opening events, described by the ZA-loop opening contact distance. Dots have been colored according to their membership in the metastable open state characterized by the MSM, with black representing a low probability. Dashed lines indicate a distance of 0.35 nm as a reference of h-bond contacts. Note that for BRD1 the sporadic and narrow peaks are very frequent, and eventually show a certain degree of metastability. (**b**) The fast opening is mainly related to a switching interaction from the Val591-Asp608 backbone h-bond to the Ser592-Asp608 h-bond. (**c**) Empirical free energy landscape composed by h-bond 1 and the ZA-loop backbone contacts with the conserved aspartate. Distribution of the minimum distance between the side chains of Ser592 and Asp608 for the two states. (**d**) Top view of the fast/slow open state structures highlighting that the slow process is related to an outward-to-inward displacement of the ZA-loop, which is captured by the h-bond 1 distance.

4. Analysis of pocket volumes

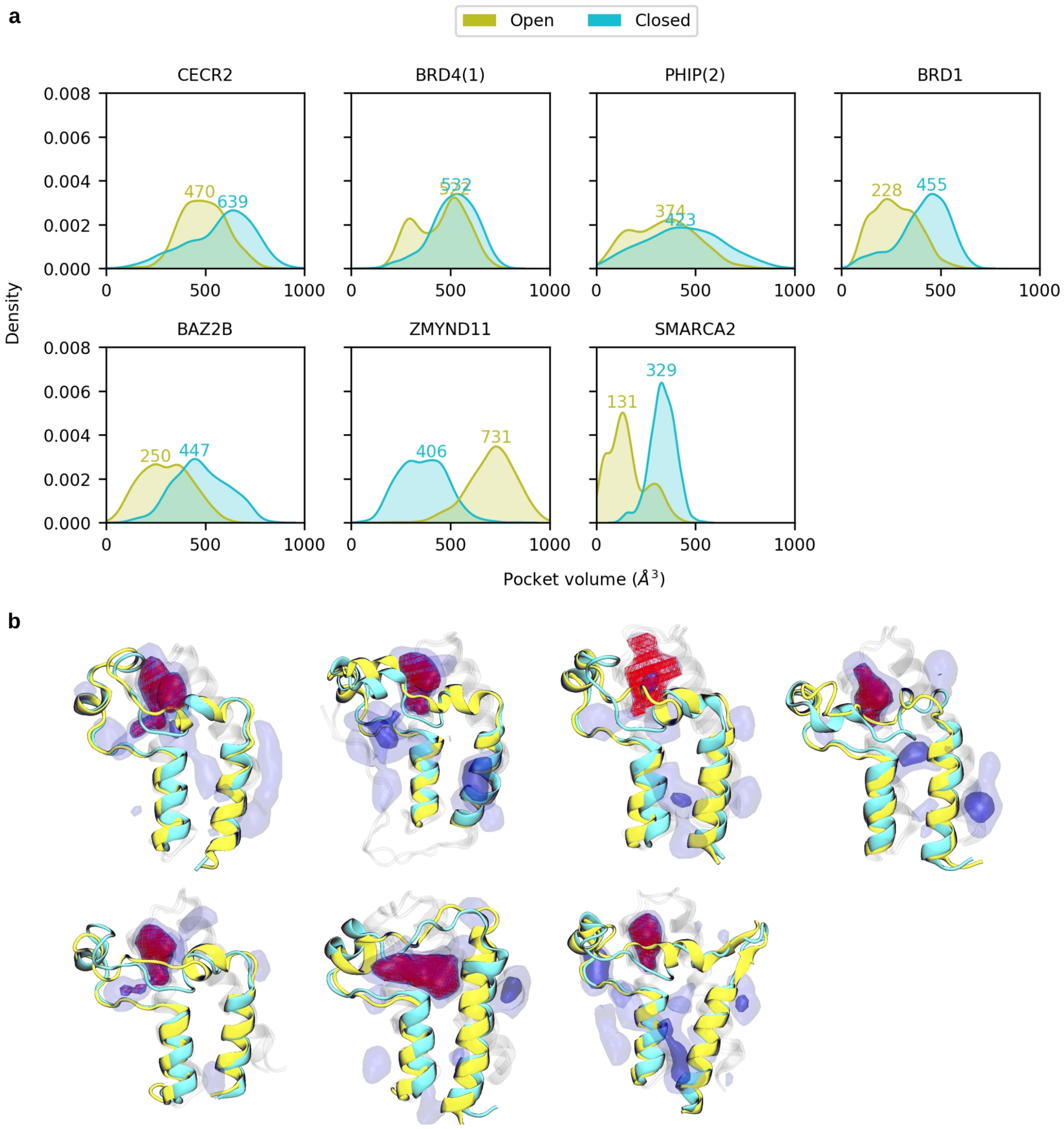

Supplementary Figure 15. Shrinking of the acetyl-lysine pocket upon the opening process. (**a**) Volume of the acetyl-lysine pocket of each BD evaluated with 1.000 structures of the closed state (cyan) and the open state (yellow). The mode of each kernel density estimate is shown as a colored number. (**b**) Visual representation of the acetyl-lysine pockets –shown in red– and the two metastable states for each BD. Note that for ZMYND11 we selected the principal cryptic pocket since the closed state is never fully formed and thus the acetyl-lysine pocket is not defined. TRIM28 is not included in this analysis given the lack of noticeable pockets in the closed state.

	CECR2		BRD4(1)		PHIP(2)		BRD1	
	Open	Closed	Open	Closed	Open	Closed	Open	Closed
Samples	999	997	999	997	967	896	930	974
Mean	493	574	451	517	339	437	272	413
SD	114	166	127	115	160	193	110	128
Min	75	29	163	103	27	25	72	46
25%	409	458	328	447	206	300	186	344
Median	488	604	478	527	343	435	263	438
75%	572	697	548	599	456	577	355	509
Max	815	973	739	779	793	971	601	675

	BAZ2B		ZMYND11		SMARCA2	
	Open	Closed	Open	Closed	Open	Closed
Samples	912	995	997	973	524	991
Mean	303	478	711	362	157	334
SD	124	135	121	118	96	65
Min	32	101	173	57	25	113
25%	205	384	637	271	92	296
Median	296	470	721	363	140	335
75%	395	575	791	446	210	378
Max	623	846	1034	839	428	540

Supplementary Table 5. Volume distribution of the acetyl-lysine pocket ($Å^3$) of each BD evaluated with 1000 representative structures of the open and closed states. The number of samples correspond to volumes above 0 $Å^3$. Volumes for ZMYND11 refer to the principal cryptic pocket since the acetyl-lysine pocket is not defined. Note the high standard deviation (SD) of the pocket volume of PHIP(2) in the closed state. TRIM28 is not included in this analysis given the lack of noticeable pockets in the closed state.

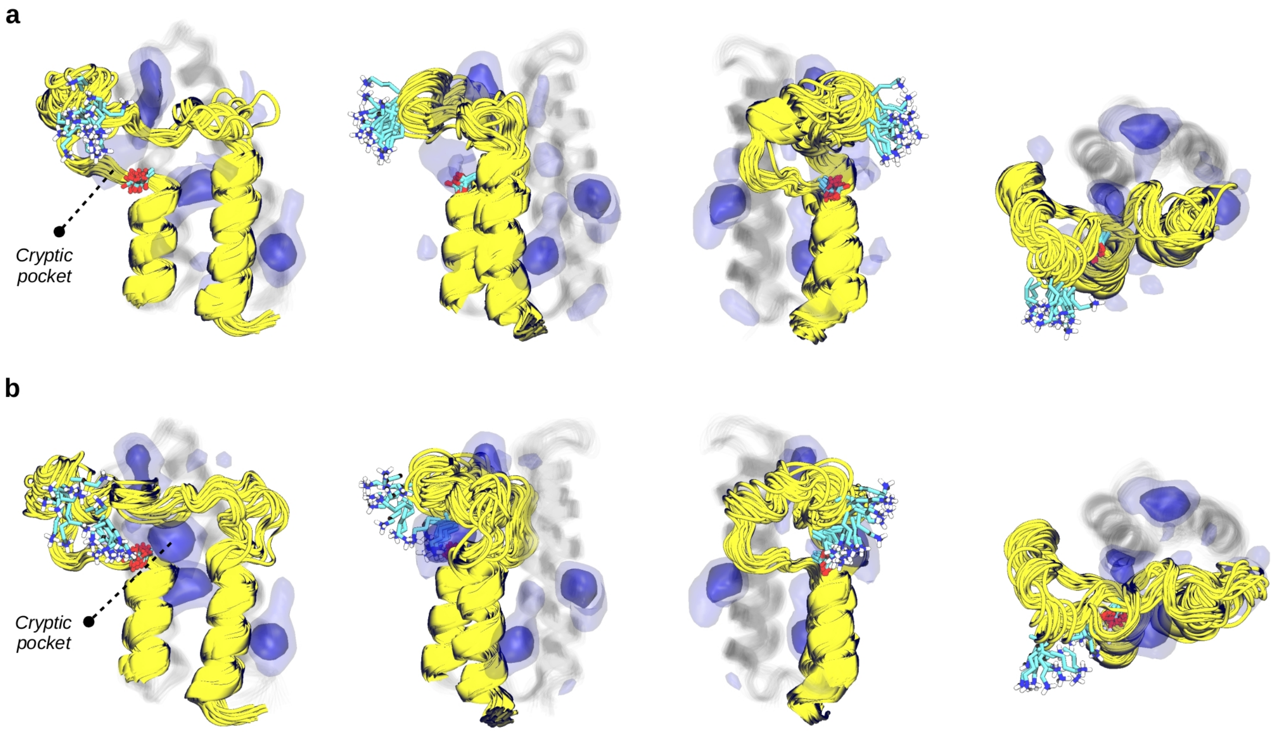

Supplementary Figure 16. Displacement of the cryptic pocket in an alternative open state of BRD1. Different views of the cryptic pocket in the open state characterized by the MSM (**a**) and in an alternative open state that is not included in the model (**b**). Note that in the alternative state the pocket is displaced towards the α_Z and α_A helices and that a lysine residue (Lys594, shown in cyan) interacts with the conserved aspartate (Asp608). Pocket frequency maps are represented by blue isosurfaces given at 0.25 (light) and 0.50 (intense) isovalues.

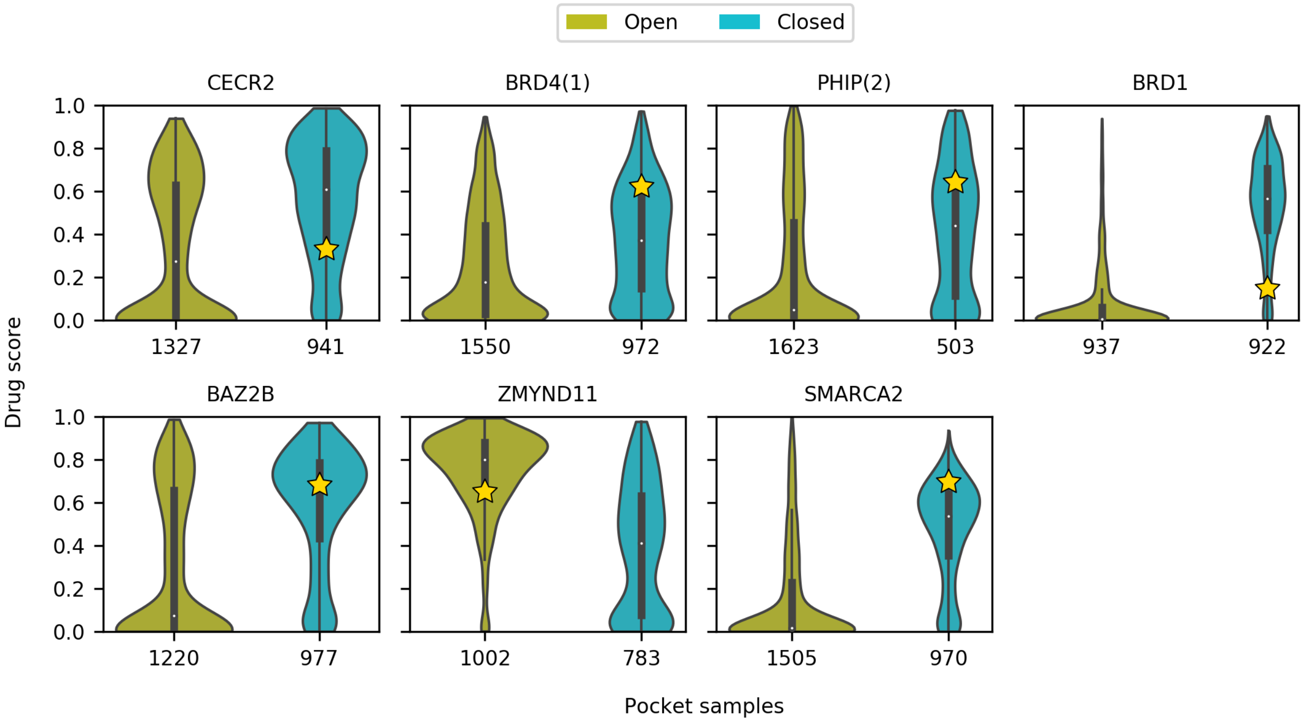

Supplementary Figure 17. Druggability scores for the cryptic pocket in the open state and the acetyl-lysine pocket in the closed state. Violin plots of Fpocket druggability scores, evaluated with 1.000 structures of the closed state (cyan) and the open state (yellow) for each BD. The distributions include different pockets that are within 0.35 nm of certain residues that we used to define the cryptic and the acetyl-lysine pockets in each state. The numbers at the x-axis indicate pocket samples in each distribution. Note that in the open state samples are generally above 1.000 as different surface pockets nearby the conserved aspartate are included. Note as well the low number of samples for PHIP(2) in the closed state, indicative of its partial obstruction. The stars represent the scores of the acetyl-lysine pocket for the crystallographic structures used in this work. For ZMYND11 the star refers to the score of the principal pocket in the open state, since the crystal structure is already open. TRIM28 is not included in this analysis given the lack of noticeable pockets in the closed state.

5. Analysis of experimental structures

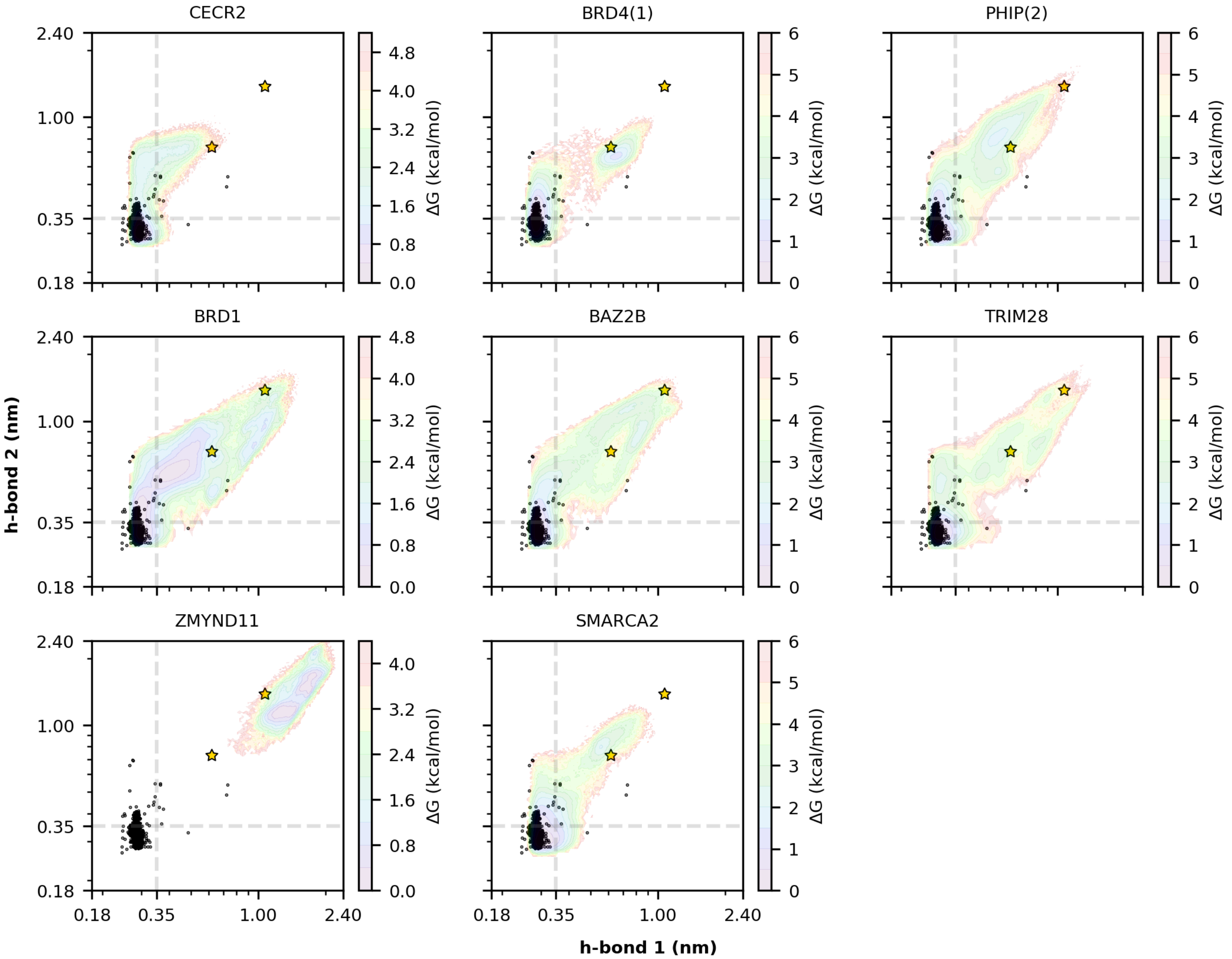

Supplementary Figure 18. Distribution of the key h-bonds in experimental structures projected onto the raw h-bond free energy landscape of each BD. All experimental structures (black dots) are obtained from the Pfam database (PF00439). The two stars indicate the crystal structures of PB1(6) and ZMYND11 (3IU6 and 4N4G) that are found in an open state. Empirical free energy maps are computed via projection of all the simulation data onto h-bond 1 and h-bond 2. Axes are given in a logarithmic scale to facilitate comparison between BDs. Dashed lines indicate a distance of 0.35 nm as an upper bound for h-bond formation. Note that there is a remarkable agreement between the distribution of experimental structures and the regions explored by our MD simulations. Note as well that ZMYND11 is an exception since it is stable in the open state.

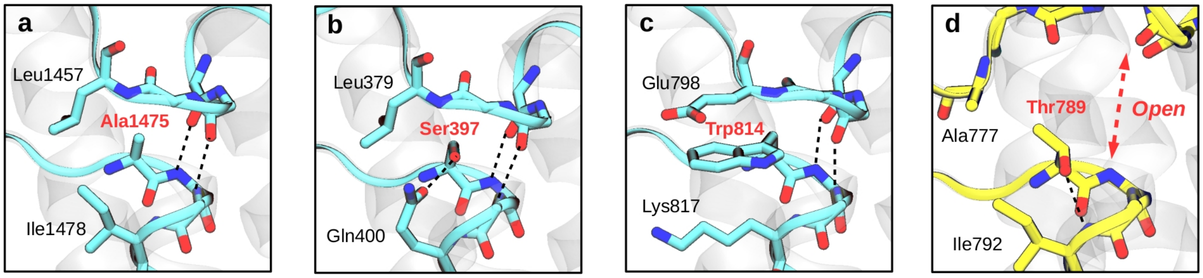

Supplementary Figure 19. Closeup of four experimental structures of BDs that do not display the conserved aspartate. (**a**) Structure of BAZ1A (PDB 5UIY) with Ala1475 in place of the conserved aspartate. Note the presence of hydrophobic residues Leu1457 and Ile1478 surrounding the alanine; (**b**) Structure of PB1(3) (PDB 3K2J) with Ser397 in place of the conserved aspartate. Note that Gln400 establishes an h-bond with the serine; (**c**) Structure of SP100 (PDB 4PTB) with Trp814 in place of the conserved aspartate. Note the presence of charged residues Glu798 and Lys817 that could establish π-interactions with the tryptophan. (**d**) Structure of PB1(6) (PDB 3IU6) with Thr789 in place of the conserved aspartate. Hydrophobic residues Ala777 and Ile792 are surrounding the threonine, which is also hydrogen bonded with the amide group of Ile792. Note that in this case the two backbone h-bonds are not formed and the ZA channel is disrupted, likely because of the bulky methyl group that threonine has in its beta carbon.

6. Nuclear magnetic resonance predictions

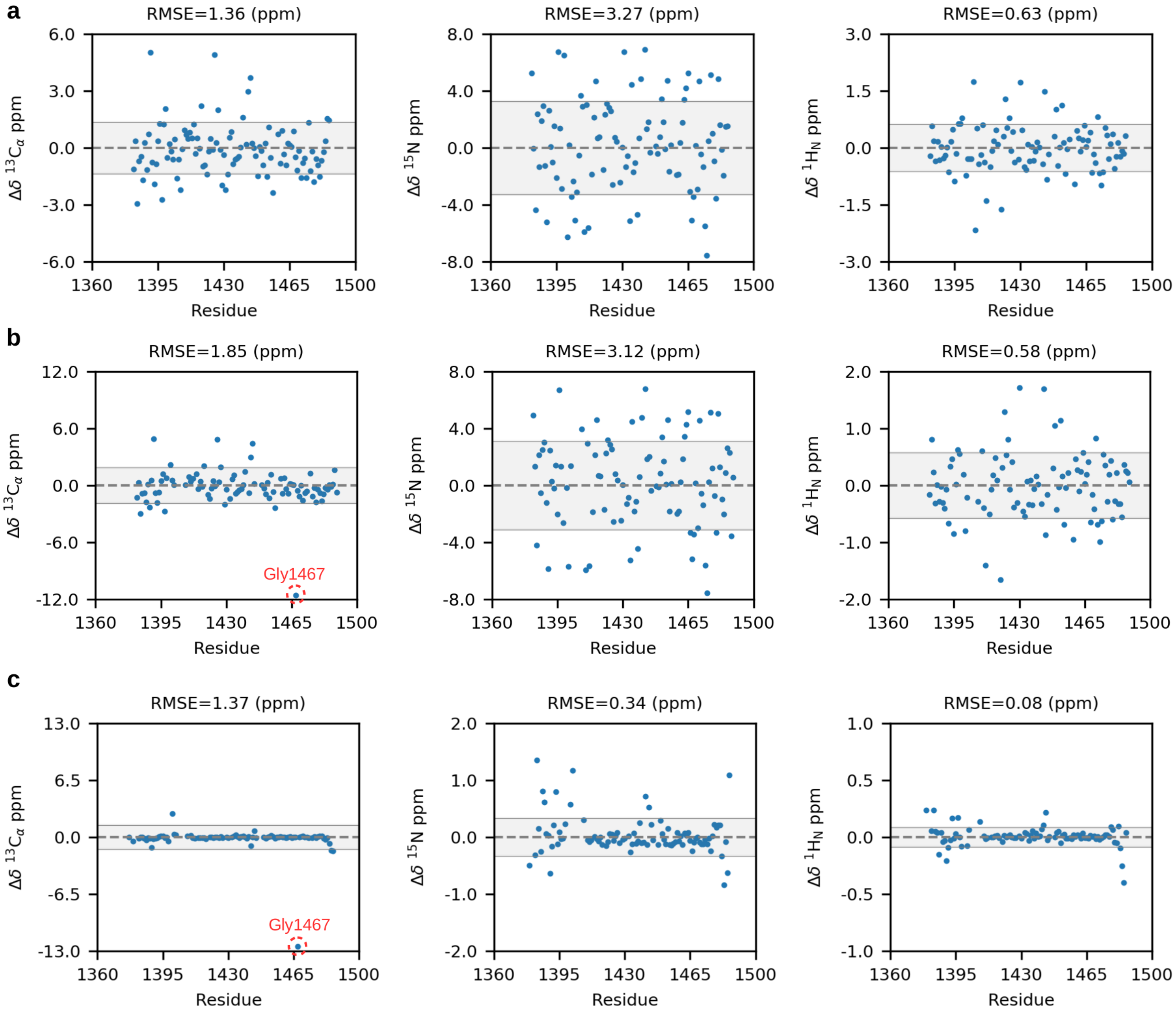

Supplementary Figure 20. Comparison of NMR SMARCA2 expectation values and experimental data. Difference between $^{13}C_{\alpha}$, ^{15}N and $^{1}H_{N}$ CAMSHIFT MSM expectation values and the experimental values of BMRB 11329 (**a**) and BMRB 27106 (**b**). The last panel (**c**) compares the two experimental sources to highlight the large deviation of Gly1467 in the $^{13}C_{\alpha}$ plot, which may arise from a misassignment or because in BMRB 27106 the hairpin has 18 extra amino acids that could interact with the glycine. The shadow areas indicate root-mean square errors (RMSE) and the residue numbering is that of PDB 5DKC.

	$^{13}C_{\alpha}$		^{15}N		$^{1}H_{N}$	
a	Residue	Δδ (ppm)	Residue	Δδ (ppm)	Residue	Δδ (ppm)
1	ILE1391	5.05	ILE1475	-7.55	SER1406	-2.17
2	ILE1425	4.91	LYS1442	6.93	LEU1405	1.75
3	ARG1444	3.71	PHE1431	6.77	ASP1430	1.73
4	TYR1443	2.96	ASN1396	6.74	GLU1420	-1.62
5	THR1384	-2.93	ASP1399	6.52	TYR1443	1.48
6	TYR1397	-2.73	SER1401	-6.28	LEU1412	-1.40
7	LEU1456	-2.35	ILE1410	-5.90	TYR1422	1.29
8	GLU1407	-2.21	LEU1412	-5.62	ASP1452	1.13
9	LEU1418	2.21	SER1474	-5.49	LEU1449	1.01
10	PHE1431	-2.20	LYS1382	5.25	ASP1473	-0.98
b	Residue	Δδ (ppm)	Residue	Δδ (ppm)	Residue	Δδ (ppm)
1	GLY1467	-11.61	ILE1475	-7.57	ASP1430	1.72
2	ILE1391	4.89	LYS1442	6.80	TYR1443	1.70
3	ILE1425	4.86	ASN1396	6.71	GLU1420	-1.66
4	ARG1444	4.44	ILE1410	-5.95	LEU1412	-1.41
5	TYR1443	2.97	ILE1390	-5.85	TYR1422	1.29
6	THR1384	-2.95	SER1401	-5.70	ASP1452	1.15
7	TYR1397	-2.75	LEU1412	-5.68	LEU1449	1.05
8	LEU1456	-2.36	SER1474	-5.62	ASP1473	-0.99
9	ALA1389	-2.33	ILE1434	-5.27	ASN1459	-0.95
10	SER1400	2.19	GLY1467	-5.19	ARG1444	-0.87
c	Residue	Δδ (ppm)	Residue	Δδ (ppm)	Residue	Δδ (ppm)
1	GLY1467	-12.49	LEU1383	1.36	ARG1485	-0.40
2	SER1400	2.71	GLY1402	1.18	ALA1484	-0.25
3	GLN1486	-1.58	GLN1486	1.10	ASN1379	0.24
4	ARG1485	-1.50	SER1483	-0.84	LEU1383	0.24
5	ALA1389	-1.18	GLN1386	0.81	TYR1443	0.22
6	LYS1442	-0.96	THR1393	0.79	ILE1390	-0.21
7	ALA1484	-0.75	HIS1441	0.72	ASN1396	0.17
8	ARG1444	0.73	ILE1390	-0.64	THR1393	0.17

9	ASN1379	-0.48	ARG1485	-0.62	GLN1386	-0.15
10	LYS1398	-0.47	MET1387	0.62	VAL1408	0.14

Supplementary Table 6. Largest deviations between $^{13}C_{\alpha}$, ^{15}N and $^{1}H_{N}$ CAMSHIFT MSM expectation values and the experimental values of BMRB 11329 (**a**), BMRB 27106 (**b**) and the comparison of the two experimental sources (**c**). The residue numbering is that of PDB 5DKC.

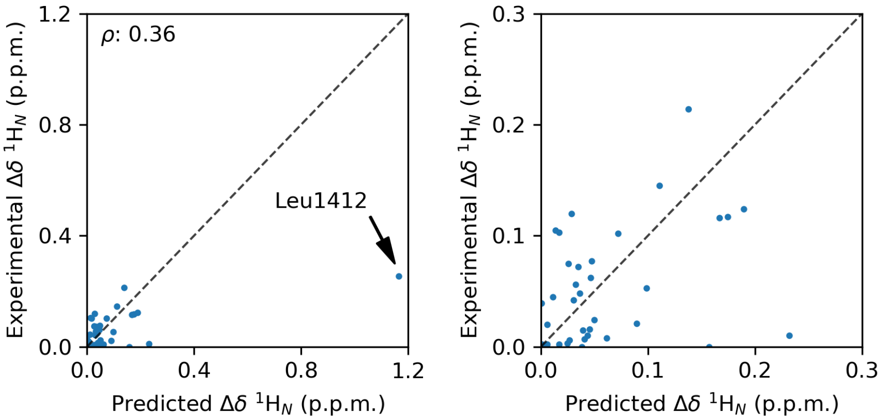

Supplementary Figure 21. Scatter plot of predicted and experimental (Morrison *et al.*) $^{1}H_{N}$ chemical shift differences for SMARCA2. Residues within the 1400 and 1440 region are displayed in the plot and used to compute the Spearman's coefficient. Note the location of residue Leu1412 in the left plot. The plot at the right shows a zoom in the 0.0-0.3 ppm region to nuance the differences.

7. References

1. Arnold, K., Bordoli, L., Kopp, J. & Schwede, T. The SWISS-MODEL workspace: A web-based environment for protein structure homology modelling. *Bioinformatics* **22**, 195–201 (2006).

2. Salomon-Ferrer, R., Case, D. A. & Walker, R. C. An overview of the Amber biomolecular simulation package. *Wiley Interdiscip. Rev. Comput. Mol. Sci.* **3**, 198–210 (2013).

3. Maier, J. A. *et al.* ff14SB: Improving the Accuracy of Protein Side Chain and Backbone Parameters from ff99SB. *J. Chem. Theory Comput.* **11**, 3696–3713 (2015).

4. Jorgensen, W. L., Chandrasekhar, J., Madura, J. D., Impey, R. W. & Klein, M. L. Comparison of simple potential functions for simulating liquid water. *J. Chem. Phys.* **79**, 926–935 (1983).

5. Heinzelmann, G., Henriksen, N. M. & Gilson, M. K. Attach-Pull-Release Calculations of Ligand Binding and Conformational Changes on the First BRD4 Bromodomain. *J. Chem. Theory Comput.* **13**, 3260–3275 (2017).

6. Eastman, P. *et al.* OpenMM 4: A reusable, extensible, hardware independent library for high performance molecular simulation. *J. Chem. Theory Comput.* **9**, 461–469 (2013).

7. Scherer, M. K. *et al.* PyEMMA 2: A Software Package for Estimation, Validation, and Analysis of Markov Models. *J. Chem. Theory Comput.* **11**, 5525–5542 (2015).

8. Wehmeyer, C. *et al.* Introduction to Markov state modeling with the PyEMMA software — v1.0. *Living J. Comp. Mol. Sci.* **1**, 5965 (2018).

9. Pérez-Hernández, G., Paul, F., Giorgino, T., De Fabritiis, G. & Noé, F. Identification of slow molecular order parameters for Markov model construction. *J. Chem. Phys.* **139**, 015102 (2013).

10. Schwantes, C. R. & Pande, V. S. Improvements in Markov State Model construction reveal many non-native interactions in the folding of NTL9. *J. Chem. Theory Comput.* **9**, 2000–2009 (2013).

11. Finn, R. D. *et al.* Pfam: The protein families database. *Nucleic Acids Res.* **42**, 222–230 (2014).

12. Theobald, D. L. & Steindel, P. A. Optimal simultaneous superpositioning of multiple structures with missing data. *Bioinformatics* **28**, 1972–1979 (2012).

13. Humphrey, W., Dalke, A. & Schulten, K. VMD: Visual molecular dynamics. *J. Mol. Graph.* **14**, 33–38 (1996).

14. McGibbon, R. T. *et al.* MDTraj: A Modern Open Library for the Analysis of Molecular Dynamics Trajectories. *Biophys. J.* **109**, 1528–1532 (2015).

15. Tribello, G. A., Bonomi, M., Branduardi, D., Camilloni, C. & Bussi, G. PLUMED 2: New feathers for an old bird. *Comp. Phys. Commun.* **185**, 604–613 (2014).

16. Kohlhoff, K. J., Robustelli, P., Cavalli, A., Salvatella, X. & Vendruscolo, M. Fast and accurate predictions of protein NMR chemical shifts from interatomic distances. *J. Am. Chem. Soc.* **131**, 13894–13895 (2009).

17. Nguyen, H., Case, D. A. & Rose, A. S. NGLview-interactive molecular graphics for Jupyter notebooks. *Bioinformatics* **34**, 1241–1242 (2018).

18. Schmidtke, P., Bidon-chanal, A., Luque, F. J. & Barril, X. MDpocket: Open-source cavity detection and characterization on molecular dynamics trajectories. *Bioinformatics* **27**, 3276–3285 (2011).

19. Vincent Le Guilloux, P. S. and P. T. Fpocket: An open source platform for ligand pocket detection. *BMC Bioinformatics* **10**, (2009).

20. Russell, R. B. & Barton, G. J. Multiple protein sequence alignment from tertiary structure comparison: Assignment of global and residue confidence levels. *Proteins Struct. Funct. Bioinforma.* **14**, 309–323 (1992).

21. Larkin, M. A. *et al.* Clustal W and Clustal X version 2.0. *Bioinformatics* **23**, 2947–2948 (2007).